Title
THE ANALYSIS OF HYPERFRAGMENTS FROM STRANGE-PARTICLE INTERACTIONS

Author
Inman, Fred W.

Publication Date
1957-06-21

UCRL 3815

UNIVERSITY OF CALIFORNIA

Radiation Laboratory

THE ANALSIS OF HYPERFRAGMENTS FROM STRANGE-PARTICLE INTERACTIONS

BERKELEY, CALIFORNIA

DISCLAIMER

UCRL-3815
Physics and
Mathematics

UNIVERSITY OF CALIFORNIA

Radiation Laboratory
Berkeley, California

Contract No. W-7405-eng-48

THE ANALYSIS OF HYPERFRAGMENTS FROM STRANGE-PARTICLE INTERACTIONS

Fred W. Inman

(Thesis)

June 21, 1957

Printed for the U. S. Atomic Energy Commission

THE ANALYSIS OF HYPERFRAGMENTS FROM STRANGE-PARTICLE INTERACTIONS

Contents

Abstract 4

Introduction

Λ^{o}-Hyperon Hypothesis 5

Negative K-Meson Interactions 6

General Characterisitcs of Events 7

Λ^{o}-Hyperon Spin 9

Binding Energy of Λ^{o} Hyperon in Hyperfragment 11

Experimental Arrangement

Preliminary Beam Studies 14

Final Geometry 17

Scanning Procedure

Method of Finding Events 18

Certification of Events 18

Follow-out of Interaction Prongs 18

Measurements

Emulsion Density 19

Shrinkage Factor 19

Range Measurements 23

Angle Measurements. 23

Charge Measurements 24

Kinematics of Decay 25

Results and Discussion

Absolute Yield of Hyperfragments 26

Hyperfragment Decay-Prong Distribution 26

Hyperfragment Range Distribution 26

Λ^{o}-Hyperon Spin 30

Fast Protons from Hyperfragment Decays 31

Identified Hyperfragments 33

$\Lambda^{H^{3}}$ 33

Identified Hyperfragments (contd)

ΛH^4 33

ΛHe^4 35

ΛHe^5 36

ΛLi^8 36

Event 195-19 37

Binding Energies of Λ^o Hyperons in Hyperfragments . . . 38

Appendices

I. Angle Error Due to Multiple Scattering 40

II. Nuclear-Track Photometer 44

III. The IBM 650 Program for Hyperfragment Analysis . . . 54

IV. Transformation to the Λ^o-Hyperon Inertial Frame . . . 59

References 63

THE ANALYSIS OF HYPERFRAGMENTS FROM STRANGE-PARTICLE INTERACTIONS

Fred W. Inman

Radiation Laboratory
University of California
Berkeley, California

June 21, 1957

ABSTRACT

Hyperfragments containing bound Λ^0 hyperons are produced in strange-particle interactions. We have studied hyperfragments that were produced by K^--meson and Σ^--hyperon interactions. Approximately 3.2% of the K^--meson interactions led to hyperfragment production. Of 14 hyperfragments that decay mesonically, we have been able to analyze eight completely and determine binding energies. Of 64 hyperfragments that decay nonmesonically, we have been able to analyze one event. The binding energies of the Λ^0 hyperons in the hyperfragments are as follows: ${}_{\Lambda}H^3$, -1.08 ± 0.72 Mev; ${}_{\Lambda}H^4$, 1.56 ± 0.65 Mev (2 events); ${}_{\Lambda}He^4$, 2.43 ± 0.64 Mev; ${}_{\Lambda}He^5$, 2.66 ± 0.39 Mev (2 events); ${}_{\Lambda}Li^8$, 5.56 ± 0.28 Mev (2 events); ${}_{\Lambda}Be^9$, 8.9 ± 2.3 Mev (nonmesonic).

INTRODUCTION

Λ^o-Hyperon Hypothesis

In 1952 Danysz and Pniewski found an event in emulsion in which a nuclear fragment from a high-energy star goes about 90 microns, apparently stops, and produces a 4-prong star with a visible energy release of about 90 Mev.[1] A number of hypothesis were proposed to account for this event. This could have been just a coincidence between a track ending and a star origin; the small probability for such a coincidence and the subsequent finding of similar events by other experimenters excludes this possibility. Perhaps the fragment from the high-energy star interacted with an emulsion nucleus; this must be ruled out because the fragment did not have enough kinetic energy to make a star consistent with the visible energy release. A third suggestion is that the fragment exists for a time in an excited nuclear state; the energy release and lifetime are inconsistent with this hypothesis. Another idea was that a π^- meson or K^- meson remained in a Bohr orbit for the necessary time and was subsequently captured by the nucleus and produced the star; the visible energy release is somewhat high for the bound π^--meson hypothesis, but the bound K^--meson hypothesis could not be ruled out. Another interesting suggestion was that the fragment contains a bound hyperon; according to the strangeness scheme, however, the Λ^o is the only hyperon that may be bound in a nucleus for the length of time necessary for observation in emulsion, since the $\Sigma^{\pm}$ hyperons would have charge-exchange in a fast reaction to Λ^o hyperons, and the Σ^o hyperons would have decayed by γ emission to Λ^o hyperons. There are two exceptions to this, namely the fragments consisting of a bound Σ^+ hyperon and proton, and a bound Σ^- hyperon and neutron. Under this hypothesis of bound Λ^o hyperon, the fragment decay proceeds because of the unstable Λ^o hyperon in the fragment. This hypothesis has proved most satisfactory in the majority of cases reported in the literature. However, Fry has reported four cases that were definitely inconsistent with the bound-Λ^o-hyperon hypothesis.[2] Two of these

cases were interpreted as examples of the hypothesis of a K^- meson in a Bohr orbit.

Negative K-Meson Interactions

The development of an enriched K^--meson beam at the Bevatron has led quite naturally to a study of unstable nuclear fragments, i. e., hyperfragments.[3] Almost every K^--meson interaction can lead to Λ^o-hyperon production. For example:

$$
\begin{aligned}
K^- + p &\rightarrow \Lambda^o + \pi^o \\
&\rightarrow \Sigma^o + \pi^o \\
&\quad\ \hookrightarrow \Sigma^o \rightarrow \Lambda^o + \gamma \\
&\rightarrow \Sigma^{\pm} + \pi^{\mp} \\
&\quad\ \hookrightarrow \Sigma^{\pm} + \begin{pmatrix} n \\ p \end{pmatrix} \rightarrow \Lambda^o + \begin{pmatrix} p \\ n \end{pmatrix}
\end{aligned}
$$

$$
\begin{aligned}
K^- + n &\rightarrow \Lambda^o + \pi^- \\
&\rightarrow \Sigma^o + \pi^- \\
&\quad\ \hookrightarrow \Sigma^o \rightarrow \Lambda^o + \gamma \\
&\rightarrow \Sigma^- + \pi^o \\
&\quad\ \hookrightarrow \Sigma^- + p \rightarrow \Lambda^o + n.
\end{aligned}
$$

Interactions of three or more bodies may also contribute to Λ^o-hyperon production. Some of these Λ^o hyperons are then found to be bound in nuclear fragments; these are the events we observe. Because of the mode of production, we do not expect any hyperfragments of the type discussed previously in which a K^- meson remains in a Bohr orbit for a sufficiently long time.

As we saw above, Σ^--hyperon interactions also can lead to Λ^o-hyperon production, therefore we look for hyperfragments from Σ^--hyperon stars as well as from K^--meson stars.

General Characteristics of Events

The range distribution of hyperfragments is strongly peaked toward short ranges. Fry, Schneps, and Swami find that more than half of the hyperfragments from high-energy π^--meson and proton stars have ranges of less than 10 microns.[4] This suggests that, in general, it is impossible to make any charge or mass determinations on the hyperfragment track itself. For such cases the analysis must be carried out on the decay-product tracks. For those few hyperfragments with sufficiently long range, a δ-ray count can be used to measure the charge of the hyperfragment. Still fewer hyperfragments have ranges that are great enough to allow a mass determination by the usual methods employing measurements of range, ionization, and multiple scattering. These charge and mass determinations can then be compared with those obtained from the analysis of the decay products.

A natural classification of hyperfragments into two groups has become common practice--namely, those which decay by π^--meson emission, and those which decay without charged π-meson emission. Although these hyperfragment decay modes are usually referred to as "mesonic" and "nonmesonic", respectively, we should remember that the second group includes the decays from which neutral π mesons are emitted.

The decay modes of the free Λ^0 hyperon are

$$\Lambda^0 \rightarrow \pi^- + H^1 + 37.14 \text{ Mev}$$

and

$$\Lambda^0 \rightarrow n + \pi^0 + 40.43 \text{ Mev.}$$

One expects some of the hyperfragments--particularly the lighter hyperfragments--to appear as if the Λ^0 hyperon decays essentially free of the residual fragment. In practice, this group of events is most amenable to analysis if the "free" decay of the Λ^0 hyperon is by the charged mode. Such hyperfragments usually have three prongs from their decay: a π^- meson, a proton, and the recoil fragment. This family of hyperfragment decays can be written as

$$_{\Lambda}Z^{A} \rightarrow \pi^- + H^1 + Z^{A-1} + Q.$$

Measuring ranges and balancing momentum is sufficient in many of these events to allow unambiguous identification of the hyperfragment. The Q of the decay reaction is determined from the kinematics. Subtraction of Q from 37.14 Mev gives the binding energy of the Λ^o hyperon in the hyperfragment.

The group of events in which the Λ^o hyperon decays essentially free and by the neutral mode is probably missed in most cases, because these decays usually lead to only one short prong and are easily confused with scatters. This type of decay reaction can be written in general form as

$$_{\Lambda}Z^{A} \rightarrow \pi^o + n + Z^{A-1} + Q.$$

For the above two cases, we have assumed not only that the Λ^o hyperon decays essentially "free" of the residual fragment, but also that the pion and nucleon are not captured by the residual fragment. A different classification of events is thus suggested in which the pion and (or) the nucleon from the "free" Λ^o-hyperon decay may be captured by the residual nucleus. This class of events may or may not be characterized by pion emission, depending on whether or not the pion is absorbed by the residual fragment. The visible energy release in this type of decay can be high if the pion is absorbed.

The hyperfragment can decay without the creation of a real pion. The Λ^o hyperon can interact with a nucleon in the fragment through a virtual pion state according to the slow reactions

$$\Lambda^o + \binom{n}{p} \rightarrow n + \binom{n}{p} + 175.47 \text{ Mev.}$$

This virtual-pion process becomes increasingly important for heavier hyperfragments. Excluding neutral pion emission, nonmesonic hyperfragment decays can result in two ways; by the above virtual-pion process, and by absorption of the pion from the "free" decay of the Λ^o hyperon. The latter process alone is unsatisfactory to account for the experimental ratio of mesonic to nonmesonic decays.[5,6] One can at least qualitatively see why the virtual-pion process becomes more

important for heavier hyperfragments by considering the Pauli exclusion principle. For a heavy hyperfragment, the proton from the Λ^o-hyperon decay generally does not have enough kinetic energy to reach the higher, unfilled energy levels of the nucleus. This has the effect of decreasing the transition probability for this "free" Λ^o-hyperon-decay process. The virtual-pion process then predominates.

Λ^o-Hyperon Spin

Information concerning the spin of the Λ^o hyperon should be available from hyperfragment studies. For the class of hyperfragments characterized by the decay reaction

$$\Lambda Z^A \rightarrow \pi^- + H^1 + Z^{A-1} + Q,$$

one can study the angular distribution of the

$$\Lambda^o \rightarrow \pi^- + H^1 + Q^1$$

decay.[7, 8] If one assumes that the pion and proton are little affected by the nucleus, then the vector sum of the momenta of the pion and the proton gives the momentum of the Λ^o hyperon. Therefore one can plot the number of events vs intervals of cos θ, where θ is the angle between Λ^o-hyperon momentum and pion momentum in the inertial frame of the Λ^o hyperon. This distribution is to be compared with expected distributions for various Λ^o-hyperon spin assignments. These studies have led to a spin assignment of 3/2 or greater. Figure 1 shows such an angular distribution.[9] This distribution includes our events. As we will see, this spin assignment is in disagreement with other considerations.

We previously discussed the virtual-pion decay mode. This mode has been studied in analogy with the familiar internal-conversion process.[10] A study of the angular-momentum dependence of this process permits a calculation of the ratio of mesonic to nonmesonic decays. This ratio can then be compared to the experimental ratio. Such a comparison suggests a Λ^o-hyperon spin of 1/2. A revised calculation by Ruderman and Karplus suggests even more strongly a

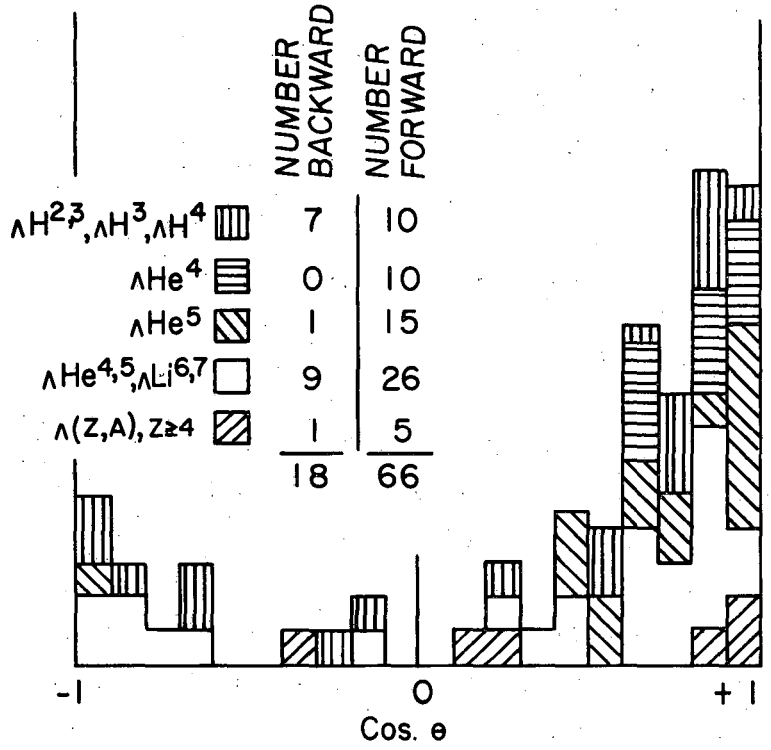

Fig. 1. Angular distribution of π^- mesons from Λ^o-hyperon decays in hyperfragments, as compiled by Setti, Slater, and Telegdi;[9] θ is the angle between the pion momentum and the Λ^o-hyperon momentum in the inertial frame of the Λ^o hyperon.

spin of 1/2 for the Λ^o hyperon.[11] The evidence from the Ruderman and Karplus considerations seems the stronger, so that one looks for difficulty in the angular-distribution studies. It is now felt that one is not justified in assuming that the pion and proton from the Λ^o-hyperon decay are little affected by the nucleus. Indeed, if one examines the apparent Q values of the Λ^o-hyperon decays, as calculated from the pion and proton energies and momenta, it becomes clear that a rather strong interaction exists between the proton and pion and the residual nucleus.

Binding Energy of Λ^o Hyperon in Hyperfragment

For those cases in which a complete analysis is possible, one can determine the decay modes of the hyperfragments and the binding energies of the Λ^o hyperons in the hyperfragments. The experimental data to September 1956 have been surveyed and summarized by Filipkowski, Gierula, and Zielinski.[12] This survey represents the experimental findings at the time our study was begun. The reader is referred to this paper for a comprehensive bibliography of experimental work. According to their selection criteria they report the following decay schemes:

${}_\Lambda H^3$ (10 cases)	1. ${}_\Lambda H^3 \rightarrow He^3 + \pi^-$	4 cases
	2. ${}_\Lambda H^3 \rightarrow H^2 + H^1 + \pi^-$	3 cases
	3. ${}_\Lambda H^3 \rightarrow Z H^1 + n + \pi^-$	3 cases
${}_\Lambda H^4$ (9 cases)	1. ${}_\Lambda H^4 \rightarrow He^4 + \pi^-$	6 cases
	2. ${}_\Lambda H^4 \rightarrow He^3 + n + \pi^-$	3 cases
${}_\Lambda He^4$ (3 cases)	1. ${}_\Lambda He^4 \rightarrow He^3 + p + \pi^-$	2 cases
	2. ${}_\Lambda He^4 \rightarrow H^2 + 2H^1 + \pi$	1 case
${}_\Lambda He^5$ (4 cases)	1. ${}_\Lambda He^5 \rightarrow He^4 + H^2 + \pi^-$	4 cases
${}_\Lambda Li^7$ (1 case)	1. ${}_\Lambda Li^7 \rightarrow Be^7 + \pi^-$	1 case

The binding energies of the Λ^0 hyperons are also given:

Hyperfragments	B_Λ (Mev)	Number of cases
$_\Lambda H^3$	0.5 ± 0.3	10
$_\Lambda H^4$	1.6 ± 0.4	8
$_\Lambda He^4$	1.6 ± 0.4	4
$_\Lambda He^5$	2.5 ± 0.3	4
$_\Lambda Li^7$	4.4 ± 0.7	1
$_\Lambda C^{11}$	14.6 ± 6	1

Another survey is being carried out by Levi Setti, Slater, and Telegdi.[9] (Approximately 10% of the hyperfragments listed below were contributed by us.) Preliminary results have been presented by these workers at the Seventh annual Rochester Conference on High-Energy Physics. They report the following hyperfragments and respective binding energies:

Hyperfragment	B_Λ (Mev)	Error	Number of events
$_\Lambda H^{2,3}$	-0.31	0.36	5
$_\Lambda H^3$	0.25	0.31	9
$_\Lambda H^4$	1.44	0.20	21
$_\Lambda He^4$	1.70	0.24	9
$_\Lambda He^5$	2.56	0.17	15
$_\Lambda Li^7$	4.17	0.62	2
$_\Lambda Li^8$	5.2	1.0	1
$_\Lambda Be^8$	5.9	0.5	1
$_\Lambda Be^9$	6.13	0.33	3

The errors listed do not include systematic errors, i.e., the error in the Q value of the free Λ^0-hyperon decay and any error in the range-energy relation. The binding energies of the above two surveys are calculated on the basis of 36.9 Mev for the Q value of the free Λ^0-hyperon decay.

In this survey work the authors present additional interesting data. They have presented the angular distribution of the pions with respect to the Λ^{o}-hyperon direction at the moment of decay. This is shown in Fig. 1. As mentioned earlier, this angular distribution suggests a spin of 3/2 or higher for the Λ^{o} hyperon. The forward-backward asymmetry in the distribution is quite interesting. This asymmetry seems to depend on the type of hyperfragment one is considering. There is a small asymmetry for the hydrogen hyperfragments and a large asymmetry for the helium hyperfragments.

An assumption is involved in compiling binding-energy information. If hyperfragments can exist in an excited nuclear state for a time on the order of the hyperfragment decay time, then the hyperfragments will decay in a fraction of the cases from the excited state, and in the rest of the cases from the ground state. Two binding energies will result, and if the energy separation between the nuclear states is smaller than the typical binding-energy errors, the existence of the excited nuclear state may be masked.

EXPERIMENTAL ARRANGEMENT

Preliminary Beam Studies

Particles of momentum 435 Mev/c from the 73°, 0.5-by-1-by-3.5-inch copper target are magnetically deflected by the Bevatron field and pass through a slot in the magnet yoke, as indicated in Fig. 2. We took advantage of this "beam" of particles of 435 Mev/c and attempted a separation of the K^--meson component of this beam. As a preliminary study, we exposed two stacks in order to determine the nature of the beam as it came from the magnet slot of the Bevatron. The 2Q stack, which consisted of 85 G.5 emulsion pellicles 3 by 6 inches by 600 μ, was exposed at the focal point of the quadrupoles. The target was bombarded with 6.2-Bev protons. Negative pions formed the major component of the beam. The π^-/K^- ratio was 3000/1.

The S stack, which consisted of 162 4-by-6-inches-by-600μ G.5 emulsion pellicles, was exposed at the energy-degrader position, which roughly corresponded to the focal point of the quadrupoles. The total flux was 6×10^3 cm^{-2} particles per 10^{10} protons on the copper target. Figure 3 indicates the beam contour at the energy-degrader position.

Both the 2Q and the S stacks were area-scanned in the region of expected K^--meson stoppings. The pions passed through the stack at essentially minimum ionization and--along with their interaction products--constituted the only background problem. The length of exposure was determined by the pion flux. Negative K mesons were found, and from their range it was possible to determine the momentum spread and distribution of the beam from the beam port. The mean momentum of K^- mesons thus determined was 427 Mev/c. The K^- mesons lose some energy coming through the Bevatron structure. This accounts for the decrease in momentum in passing from the vacuum tank of the Bevatron to the region outside the Bevatron.

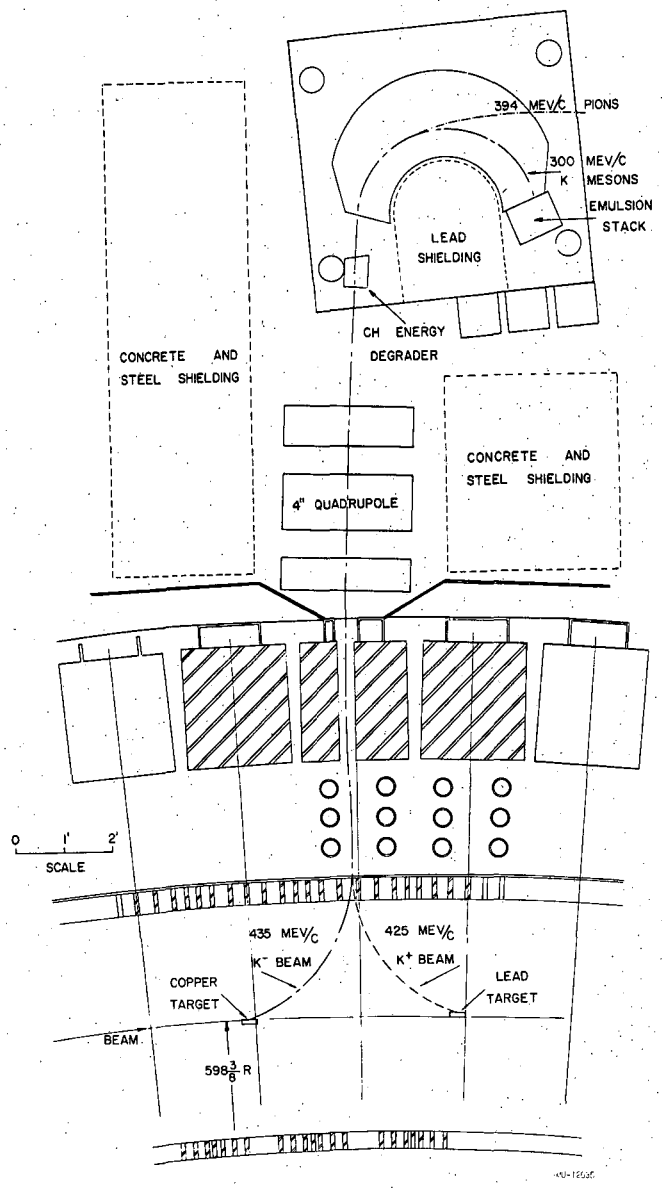

Fig. 2. Plan drawing of the experimental arrangement at the Bevatron.

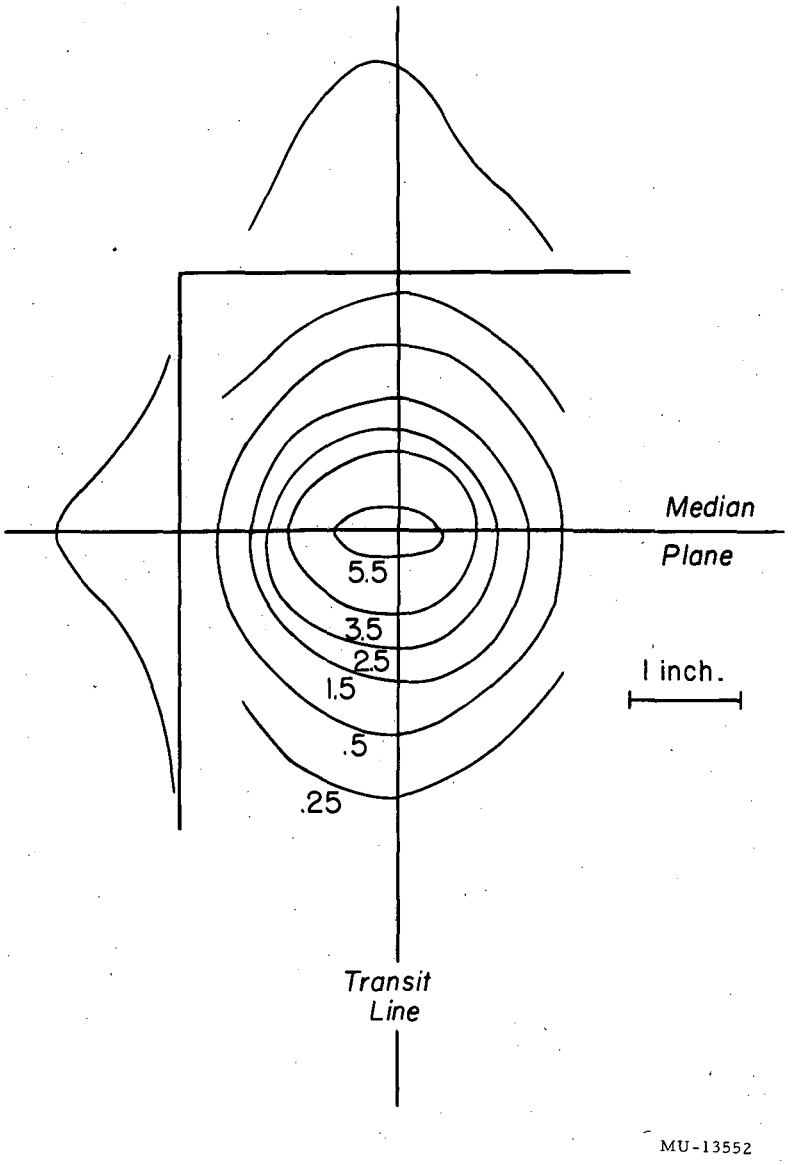

Fig. 3. Beam flux at the degrader position. The flux is given in units of 10^4 particles per cm^2 per 10^{11} protons on the Bevatron target.

Final Geometry

The preliminary beam studies described above allowed us to design a system which effects the separation of the K^- mesons from the π^- mesons. Referring again to Fig. 2, we see a CH energy degrader, which was used to introduce a momentum difference between the K^--meson and π^--meson components of the 427-Mev/c beam. Upon traversing the degrader, the pions and K^- mesons were reduced to momenta 394 Mev/c and 300 Mev/c, respectively. The analyzing magnet deflected 300-Mev/c particles through approximately 180^o and into the emulsion stack. The separation between the peaks of the separated pion and K^--meson beams was 19 inches at the stack position. The momentum gradient at the stack position was 1.6 Mev/c per cm, with a ± 2% dispersion in momentum.

The background at the stack position was composed of muons (80%), electrons (10%), and pions (10%). The ratio of minimum tracks to K^- mesons entering the stack was 800:1. The muons are minimum-ionizing and weakly interacting, and do not appreciably hinder scanning. More than 95% of the particles that are twice minimum ionizing and enter within 10^o to the expected beam direction are K^- mesons.

The 1U stack, which consisted of 120 3-by-6-inch-by-600-μ G.5 emulsion pellicles, was exposed in the stack position and was used to carry out a preliminary evaluation of the experimental arrangement, the results of which are quoted above. For this run the degrader was 18.4 cm^{-2} thick.

The 2B stack consisted of 240 9-by-12-inch-by-600-μ G.5 emulsion pellicles and was used in the final exposure. The degrader for this run was 19.4 cm^{-2} thick. The hyperfragments for this study came from the 1U and 2B stacks. A few hyperfragments were found in the 2Q and S stacks also, but we lacked accurate shrinkage-factor information, and did not attempt analysis of these few.

SCANNING PROCEDURE

Method of Finding Events

The scanning program devised for the final exposures at the stack position (Fig. 1) was designed to accommodate a number of studies. Scanners were instructed to scan along a line parallel to the plate edge into which the beam enters. This line was located a few millimeters in from the beam edge. All tracks of about twice minimum ionization and having a direction within 10° of the average direction of minimum-ionizing tracks in that region were followed until they interacted or decayed.

Certification of Events

All K^--meson interactions (in flight or at rest) and decays were looked at by a physicist while the event was still in the microscope of the scanner who found the event. For interactions in flight, the scanners were instructed to make an opacity measurement at the pick-up point and at the interaction point. This helped the physicist in his certification of the event. The presence of hyperfragments and hyperons from interactions (and pions from interactions at rest) guarantees that the event is a K^--meson interaction. Stars at rest that have six or more prongs are most certainly due to K^--meson interactions.

Follow-out of Interaction Prongs

The scanners were instructed to follow all prongs from K^--meson interactions until they stopped or left the pellicle, with the exception that prongs from one- or two-prong stars that ionized more than four times minimum were followed out even though they passed into other pellicles. This method of following out prongs introduces a bias against long-range hyperfragments. This does not seem to be serious, however. All the prongs from a group of 100 K^--meson stars were followed out until they stopped, decayed, or interacted. This search did not reveal any additional hyperfragments. From this fact and from the range distribution of the hyperfragments we conclude that we miss less than 10% of the hyperfragments because of this bias. The time spent on following out all prongs from K^--meson interactions does not seem justified.

MEASUREMENTS

Emulsion Density

The usefulness of range measurements in emulsion depends critically upon the emulsion density at the time of exposure, and this density should be carefully determined. At the time of the disassembly of the 2B stack, small pieces of emulsion were cut from every twentieth pellicle. The density of each of these twelve pieces of unprocessed emulsion was determined by displacement in carbon tetrachloride. These twelve density values are listed in Table I. There appears to be a small variation in density among the different emulsion batches. These variations are negligible for the purpose of this work. The mean value of the twelve densities in Table I is 3.815 cm^{-3}.

Shrinkage Factor

Precise range measurements for steep tracks are dependent upon precise knowledge of the shrinkage factor. The thickness of each of the 240 processed pellicles of the 2B stack was measured twice at each of three places. This gave six thickness measurements for each pellicle, and a total of 1, 440 thickness measurements for the complete stack. This information, along with the mean thickness of the unprocessed emulsions, permitted accurate determination of the shrinkage factor. Two methods are available for determining the unprocessed thickness of the emulsion. The thickness of the assembled stack was measured with calipers. This measured the pellicle thickness plus the air space between pellicles. The value obtained from this measurement was 651.6 microns for the mean thickness of pellicle plus air space. Another method, which measures the mean pellicle thickness only, is the one that was used in determining the shrinkage factor. The area of each of the processed emulsions was measured carefully. The unprocessed emulsions were weighed immediately after disassembly of the stack. The areas of the pellicles, the weight of the stack, and the density of the emulsion allowed the calculation of the original mean pellicle thickness,

TABLE I

Emulsion Density of Stack 2B

Manufacturer's emulsion batch number	Denisty ($g\ cm^{-3}$)	Mean density ($g\ cm^{-3}$)
Z9804	3.8202	3.8212
	3.8222	
Z9806	3.8110	3.81415
	3.8173	
Z9808	3.8182	3.8155
	3.8128	
Z9809	3.8288	3.8303
	3.8318	
Z9810	3.8002	
	3.8066	3.80307
	3.8024	
Z9811	3.8065	3.8065
Mean Density	3.81483 $g\ cm^{-3}$	

$$t = \frac{WA}{d},$$

where t is the mean pellicle thickness, W is the mean pellicle weight, A is the mean pellicle area, and d is the emulsion density. This method gave 634.61 microns for the mean pellicle thickness. This indicated a mean air space of 17.0 microns.

The emulsion for the 2B stack was manufactured in six batches (see Table I). In addition, our darkroom facilities necessitated dividing the stack into four batches for processing. One expects different shrinkage factors for different processings and for different emulsion batches. The mean processed thicknesses are catalogued according to the emulsion batch and process batch in Table II. It appears difficult to separate the shrinkage-factor dependence upon emulsion batch. This dependence is certainly smaller than the dependence upon process batch. For this reason we consider the shrinkage factor a function of process batch only. In Table III we express the shrinkage factors relative to process batch. A weighted mean is taken among the emulsion batches. Then we obtain four relative shrinkage factors corresponding to the four process batches. If n is the number of pellicles, S is the shrinkage factor, and t is the mean processed-pellicle thickness, then the total stack thickness, T is given by

$$T = n_a S_a t_a + n_b S_b t_b + n_c S_c t_c + n_d S_d t_d.$$

Using the stack thickness previously determined, along with the measured mean thicknesses and the relative shrinkage factors, we determine S_d to be 2.111. The other shrinkage factors follow immediately:

$$S_a = 2.374,$$

$$S_b = 2.230,$$

$$S_c = 2.305,$$

$$S_d = 2.111.$$

The 1,440 thickness measurements of the processed pellicles are used to adjust the above shrinkage factors as the pellicles swell or shrink

TABLE II

Processed emulsion thicknesses

Emulsion batch	Process batch			
	a	b	c	d
Z9804		278.1 (23)		294.0 (17)
Z9806	271.4 (30)			300.0 (12)
Z9808	271.6 (30)			310.5 (12)
Z9809		275.9 (24)		294.3 (16)
Z9810		286.9 (12)	279.3 (13)	303.3 (13)
Z9811		288.9 (13)	275.0 (11)	301.9 (14)

The figures in parenthesis indicate how many pellicles in that category.

TABLE III

Relative Shrinkage Factors

	S_a/S_d	S_b/S_d	S_c/S_d	S_d/S_d
Z9804		1.057		1.000
Z9806	1.105			1.000
Z9808	1.144			1.000
Z9809		1.067		1.000
Z9810		1.057	1.086	1.000
Z9811		1.045	1.098	1.000
Weighted mean	1.125	1.056	1.0928	1.000

owing to humidity changes. By measuring the pellicle thickness at a given time and comparing the results of the measurement with the measurement made at the time the shrinkage factors were determined, we can adjust the shrinkage factors to correspond to the pellicle thickness at that given time. The errors in the shrinkage factors are estimated to be less than 1%.

Range Measurements

For this hyperfragment study we have used the range-energy relation of Barkas, which is believed to be accurate to better than 1% in range (except perhaps at very short ranges).[13] The precision of energy determinations from range measurements depends not only upon the accuracy of the range-energy relation, but also upon range straggling in emulsion. The following four effects are important in range straggling: (a) Bohr straggling, which is given by theory, (b) end straggling, which is important only for short tracks, (c) proportional straggling, which includes effects due to microscopic distortion, observer error, and heterogeneity of the emulsion, and (d) follow-through straggling, which arises when tracks are followed from one pellicle to another. For evaluation of straggling errors, we refer to the quantitative study that was done by Barkas, Smith, and Birnbaum.[14]

Angle Measurements

It is necessary to know as precisely as possible the direction angles of the tracks from hyperfragment decays, because--as we have suggested--the analysis of the decays depends crucially upon the kinematics. There are two sources of error in angle measurements. Multiple Coulomb scattering introduces a statistical uncertainty in the direction of the track. The rms error due to this effect is $\sqrt{\pi/4}\,\langle a \rangle$. The quantity $\langle a \rangle$ is given by the usual scattering formula;[16]

$$\langle a \rangle = \frac{K}{p\beta} \left(\frac{t}{100}\right)^{1/2} , \qquad (1)$$

where $\langle a \rangle$ is the mean angle in degrees between successive chords, t is the chord length in microns, p is the momentum in Mev/c, and

β is the velocity parameter, v/c. K is a slowly varying function of velocity which, in the region of interest, is equal to 25 in the units above. The factor $\sqrt{\pi/4}$ is derived in Appendix I.

The other kind of error to be considered in angle measurements is the observer error. For projected angles, this error depends upon how accurately a reticule can be placed along a track of finite width. This error, which we call σ_o, is inversely proportional to the length of reticule used in the measurement with proportionality constant estimated to be 17, i. e.,

$$\sigma_o = 17/t,$$

where σ_o is in degrees and t is the length in microns of reticule used for the angle measurement. If we call the multiple-scattering error σ_{ms} and assume that σ_o and σ_{ms} are independent, then

$$\sigma = \sqrt{\sigma_{ms}^2 + \sigma_o^2}$$

represents the total error on the angle determination. There is a reticule length t_m that minimizes the above error. This has been calculated in Appendix I and can be expressed as

$$t_m = 4.52\ (p\beta)^{2/3}$$

where t_m is in microns and $p\beta$ is in Mev/c. In addition, the error corresponding to this minimal condition is

$$\sigma = 6.51/(p\beta)^{2/3},$$

where σ is in degrees and $p\beta$ is in Mev/c.

For dip angles, the observer error depends upon the magnitude of the dip angle. It is determined in each case.

Charge Measurements

A δ-ray count along a nuclear track allows an estimate of the charge of the particle producing the track.[15] However, for short tracks there may be too few delta rays to give statistical certainty to the charge estimate obtained from the count. A nuclear-track

photometer has been built and has been used to aid in the charge measurements. This device essentially measures the width of the track. Measurements of track width have been utilized to make charge estimates for slow, multiply charged particles.[16, 17,] This photometer is described in detail in Appendix II.

Kinematics of Decay

In the majority of cases it is impossible to make certain identification of all the prongs from hyperfragment decays by performing measurements on the tracks themselves. Pions are identified unambiguously, but other tracks can be identified only if they have a sufficiently long range. It becomes necessary to study the kinematics of the decays in order to determine the identity of some of the prongs from these hyperfragment decays. In applying the methods of kinematics analysis, one assumes various identities for the prongs from a decay. Then the binding energy of the Λ^{o} hyperon is calculated, and if the event is colinear or coplanar the momentum unbalance is calculated. The requirements that the binding energy of the Λ^{o} hyperon be positive and that the momentum be balanced in colinear and coplanar decays, are sufficiently rigid in many cases to determine the identity of the prongs and consequently of the hyperfragment.

A program for the IBM 650 data-processing machine has been written to facilitate the kinematic analysis of hyperfragment decays. All permutations of the assumed identities for each of the decay prongs are taken into account by the IBM 650, and the relevant kinematic quantities are calculated for each set of assumptions. A more detailed discussion of the program is contained in Appendix III.

RESULTS AND DISCUSSION

Absolute Yield of Hyperfragments

From 2469 K^--meson interactions we find 64 nonmesonic hyperfragment decays and 14 mesonic decays. The absolute yield is therefore 78 hyperfragments from 2469 K^--meson interactions. This corresponds to about 3.2% of the K^--meson interactions yielding hyperfragments.

Hyperfragment Decay-Prong Distribution

The decay-prong distribution of the hyperfragments is given in Fig. 4. We have separated those hyperfragments which decay by emission of a negative pion, and represented them on the histogram as the dark region. It is seen that the largest number of prongs observed by us is six. This means that hyperfragments at least as large as carbon were found.

Hyperfragment Range Distribution

We have separated our hyperfragments into two groups in order to study the range distribution. A question has arisen, which has been of concern to us, regarding the identification of hyperfragments. Because many of the hyperfragments have very short ranges we might be confusing hyperfragments with short-range Σ^- hyperons, which produce stars when they stop and are captured. The energy spectrum of Σ^--hyperon stars has been studied, and it is found that the visible energy release is rarely above 50 Mev.[18] We consider identified hyperfragments and hyperfragments with visible energy greater than 50 Mev as one group, and plot their range distribution in Fig. 5. There are 35 events in this group. As the second group we consider those events with visible energy release less than 50 Mev, and plot their range distribution in Fig. 6. There are 29 events in this group. The similarity in range distribution of the two groups leads us to believe that there is little Σ^--hyperon contamination in our group of events.

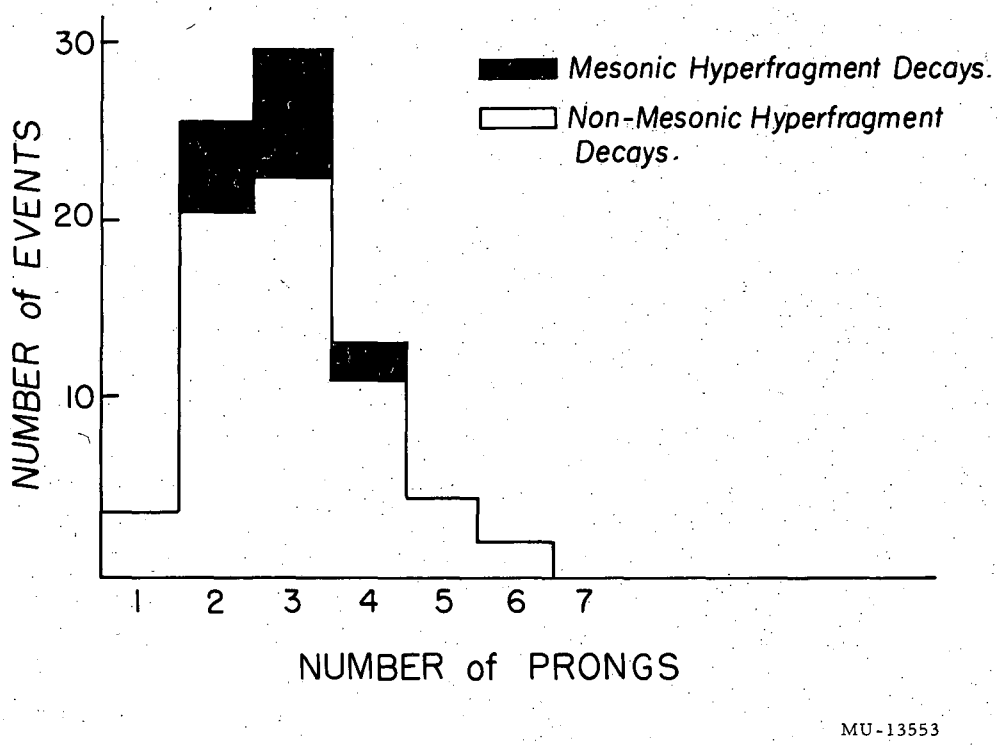

Fig. 4. Prong distribution of hyperfragment decays.

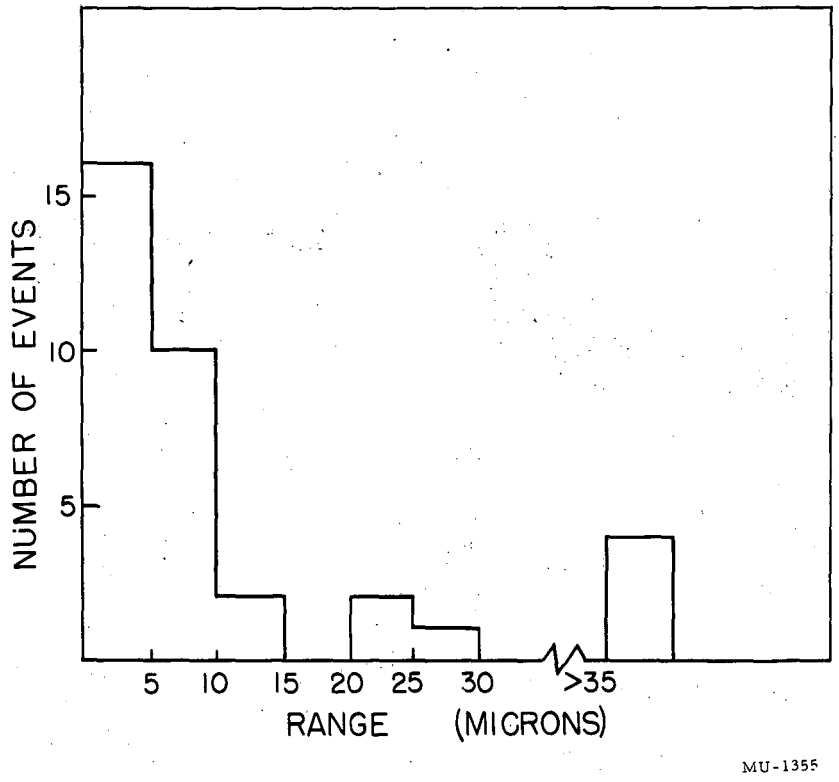

Fig. 5. Range distribution in intervals of 5 microns of hyperfragments and probable hyperfragments whose decays show > 50 Mev visible energy release.

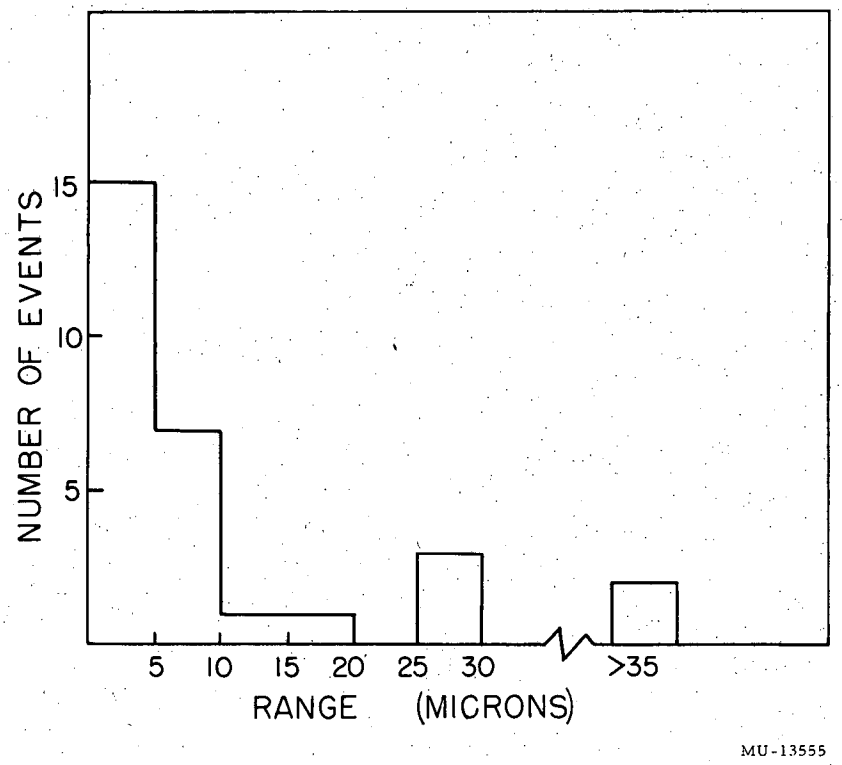

Fig. 6. Range distribution in intervals of 5 microns of probable hyperfragments whose decays show < 50 Mev visible energy release.

Λ^o-Hyperon Spin

As was mentioned earlier, the ratio of mesonic to nonmesonic helium-hyperfragment decays gives information concerning the spin of the Λ^o hyperon.[10, 11] We find three mesonic helium hyperfragments and eight nonmesonic helium hyperfragments. The number of nonmesonic helium hyperfragments was estimated by examining visually the one- and two-prong nonmesonic hyperfragment decays. The identification error is estimated to be less than 50%. This ratio certainly suggests a spin assignment of 1/2 if we consider the latest calculations by Karplus and Ruderman, in which they give revised values of $Q^{(-)}$, where $Q^{(-)}$ is the ratio of nonmesonic decays to mesonic decays, and B_Λ is the binding energy of the Λ^o hyperon in Mev. The angular-momentum state of the pion is indicated by ℓ. The ratio corresponding to $\ell=0$ fits the data best, suggesting spin 1/2 for the Λ^o hyperon.

ℓ	Expression for $Q^{(-)}$	Value of $Q^{(-)}$ for B_Λ = 2.0 Mev
0	$0.8\ B_\Lambda^{1/2}$	1.1
1	$14\ B_\Lambda^{1/2}$	20
2	$240\ B_\Lambda^{1/2}$	340
3	$4000\ B_\Lambda^{1/2}$	5600

We have also considered those hyperfragment decays which are characterized by

$$\Lambda Z^A \rightarrow \pi + H^1 + Z^{A-1} + Q.$$

We have six events of this type; three helium events and three lithium events. We form the vector sum of the pion and proton momenta and associate this sum with a Λ^o hyperon. This Λ^o-hyperon momentum is used to calculate the kinetic energy of the Λ^o hyperon in the nucleus. These kinetic energies are listed in Table IV. A transformation to the inertial frame of the Λ^o hyperon allows the calculation of the angle between the Λ^o-hyperon momentum and the pion momentum. These transformations are described in Appendix IV. In addition, we calculate the

TABLE IV

Apparent Q values of Λ^o-hyperon decays and kinetic energies of Λ^o hyperons in hyperfragments

Hyperfragment Identity	Apparent Q	Kinetic energy (Mev)
$_{\Lambda}He^4$	25.9 Mev	6.0
$_{\Lambda}He^5$	22.8	9.4
$_{\Lambda}He^5$	23.6	7.2
$_{\Lambda}Li^8$	30.2	1.7
$_{\Lambda}Li^8$	11.4	16.3
$_{\Lambda}Li^{7,8}$	27.4	3.4

momentum of the pion in the inertial frame of the Λ^o hyperon. This allows the calculation of an apparent Q value in the center-of-mass system of the Λ^o-hyperon decay. The angular distribution of the pions is given in Fig. 7, and the apparent Q values are listed in Table IV. Upon comparing our angular distribution with the angular distribution of Fig. 1 we find good agreement with the results of the world survey. The asymmetry and anisotropy of the angular distribution are not well understood. The anisotropy suggests that the interaction of the nucleon and pion with the residual nucleus is important, if the spin of the Λ^o hyperon is 1/2, as we suspect from other considerations. In summary it is generally felt that the ratio of mesonic to nonmesonic decays is the most significant measure of the Λ^o-hyperon spin. Effects other than the Λ^o-hyperon spin seem to be responsible for the anisotropy observed in the angular distribution of the pion momenta.

Fast Protons from Hyperfragment Decays

As was mentioned in an earlier section of this paper, the virtual-pion process is important for a large fraction of the hyperfragments. Considerable energy is available in this process, and we would expect fast protons to arise frequently from such hyperfragment decays.

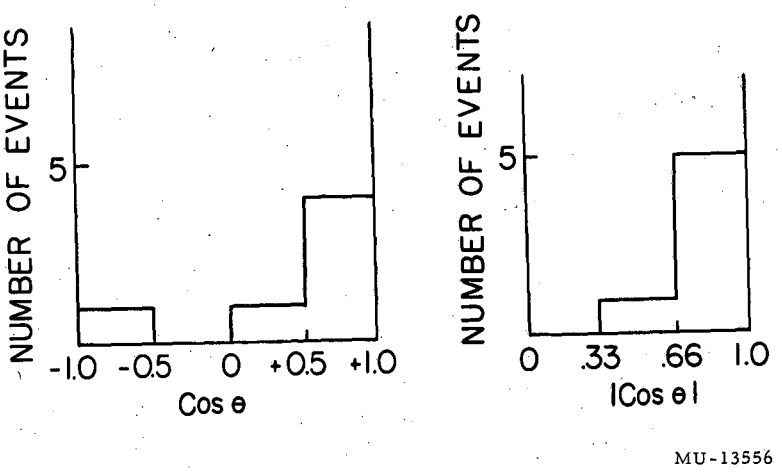

Fig. 7. Angular distribution of π^- mesons from Λ^o-hyperon decays in hyperfragments; θ is the angle between the pion momentum and the Λ^o-hyperon momentum in the inertial frame of the Λ^o hyperon.

The energy spectrum of protons with energy greater than 50 Mev is given in Fig. 8. This can be compared to the energy spectrum of fast protons from π^--meson stars.[19] In the π^--meson stars there is about 140 Mev available, while in the hyperfragment decays the available energy is about 175 Mev minus the binding energy of the Λ^0 hyperon. The two spectra are similar within the accuracy of the data. The protons from hyperfragment decay show a sharp decrease at about 85 Mev, while the protons from π^--meson stars show a similar decrease at about 70 Mev. This difference in cutoff energy is accounted for by the difference in available energy in the respective processes.

Identified Hyperfragments

In the analysis of hyperfragments we have adopted the value 37.14 ± 0.16 Mev as the Q of the free Λ^0-hyperon decay.[20]

$_\Lambda H^3$ hyperfragment. We have an event which has been interpreted as an example of the decay

$$_\Lambda H^3 \rightarrow \pi^- + He^3 + Q.$$

The range of the pion was measured, and a He^3 range was calculated by momentum balance. This calculated range was compared to the measured range and good agreement was obtained. While this is a two-body decay, it is somewhat difficult to ascertain its colinearity because the He^3 has a short range (about 9 microns). It is colinear within the errors in direction of the He^3. The energy release Q was determined to be 43.71 ± 0.70 Mev from the pion range and the momentum balance. This gives a binding energy of -1.08 ± 0.72 Mev. Although this measured binding energy is negative, it is believed that the event is correctly identified. The measured binding energy deviates from 0 by about 1 - 1/2 standard deviations. The error on the Q value is due to the range straggling of the pion.

$_\Lambda H^4$ hyperfragments. We have two events which are identified as examples of $_\Lambda H^4$ hyperfragments decaying by the mode

$$_\Lambda H^4 \rightarrow \pi^- + He^4 + Q.$$

These events are recognized by the colinearity of the decay prongs and

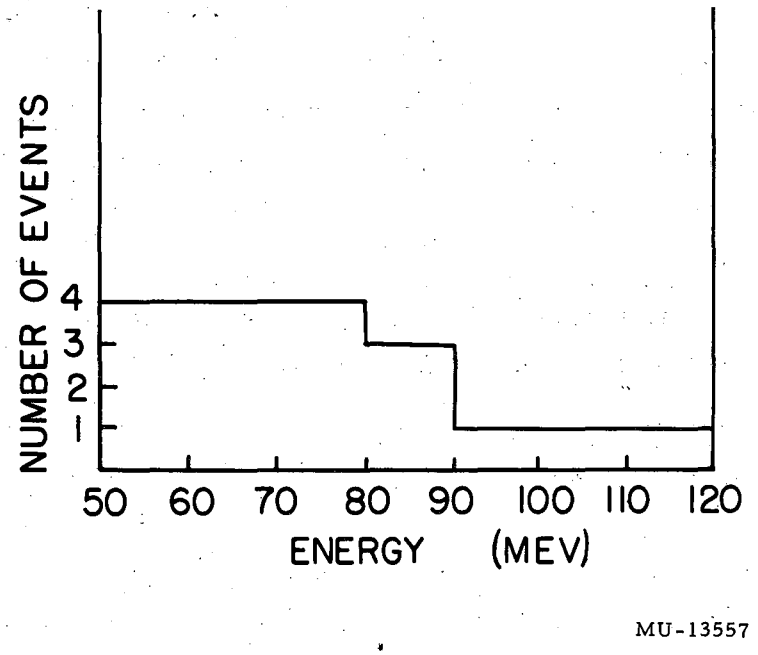

Fig. 8. Energy spectrum in intervals of 10 Mev of fast protons (T > 50 Mev) from hyperfragment decays.

the unique pion and He^4 ranges. Again, we have the same difficulty in ascertaining the colinearity of the event because of the short range of the He^4. However, all the other factors are strong evidence for the identification's being correct. The analysis consists of measuring the pion range and calculating a He^4 range by momentum balance. The calculated range is compared with the measured range, and good agreement is obtained in both cases. The calculated ranges differ from the measured ranges by less than 0.6 micron. The mean grain diameter of 0.6 micron sets an upper limit on the precision of range measurements in emulsion. The energy of the He^4 is calculated from momentum balance instead of from the measured range of the He^4, because there is a smaller energy error associated with this calculation than is found by determining the energy from the range of the He^4. The energy releases Q for the two cases are 56.44 ± 0.92 Mev and 54.32 ± 0.89 Mev. The binding energies calculated from these Q's are 0.50 ± 0.94 Mev and 2.62 ± 0.91 Mev respectively. A mean of the two values is 1.56 ± 0.65 Mev.

$_{\Lambda}He^4$ hyperfragment. This event has the decay mode

$$_{\Lambda}He^4 \rightarrow \pi^- + H^1 + He^3 + Q.$$

Many times it is difficult to distinguish between $_{\Lambda}He^4$ and $_{\Lambda}He^5$ hyperfragments. If one takes the vector sum of the pion and proton momenta and associates it with either a He^3 or a He^4, then it is possible to calculate an expected range for each of the helium isotopes. In this case, the expected ranges were 6.1 and 8.6 microns for He^4 and He^3 respectively. The measured range was 7.8 microns. Primarily on the basis of this comparison, we have said that this hyperfragment was a $_{\Lambda}He^4$. For this assignment the Q value is 34.71 ± 0.54 Mev, which gives a binding energy for the Λ^0 hyperon of 2.43 ± 0.56 Mev. The alternate mode,

$$_{\Lambda}He^5 \rightarrow \pi^- + H^1 + He^4 + Q,$$

cannot be entirely excluded, but is considerably less probable. The Q value and binding energy for it are 34.21 ± 0.54 Mev and 2.93 ± 0.56 Mev respectively.

$_{\Lambda}He^{5}$ hyperfragments. These hyperfragments are particularly interesting because they are bound mass-five nuclei. The Λ^{o} hyperon is not restricted by the exclusion principle, and can occupy a lower energy level than a corresponding nucleon could. The two cases we have decay by the mode

$$_{\Lambda}He^{5} \rightarrow \pi^{-} + H^{1} + He^{4} + Q.$$

The same technique is used in analyzing these events as was used in analyzing the above $_{\Lambda}He^{4}$ case. The vector sum of the pion and proton momenta is associated with He^{3} and He^{4} nuclei. The ranges are calculated from this and compared with the measured range. The calculated ranges for one of the events were 7.2 and 11.0 microns for He^{4} and He^{3} respectively. This is to be compared with the measured range of 7.6 microns. There is little doubt in this case. In the other event the calculated ranges were 15.6 and 9.8 microns for He^{3} and He^{4} respectively. The measured range was 11.1 microns, and agrees best with the He^{4} range. For the first case the Q was 33.44 ± 0.54 Mev and the binding energy of the Λ^{o} hyperon was 3.70 ± 0.57 Mev. For the second case the Q was 35.64 ± 0.56 Mev, and the binding energy of the Λ^{o} hyperon was 1.50 ± 0.58 Mev. A weighted mean of the two binding-energies is 2.66 ± 0.39 Mev.

$_{\Lambda}Li^{8}$ hyperfragments. 1. Event 2B91-12. This hyperfragment has a range of 781 microns and ends in a decay into a negative pion, a proton and a recoil of a few microns range. The range of the recoil is hard to determine precisely because the recoil overlaps the pion track. A δ-ray count of the hyperfragment track gives a charge of 3, indicating a lithium hyperfragment. With this particular decay mode, the only possible identities of the hyperfragment are $_{\Lambda}Li^{7}$ or $_{\Lambda}Li^{8}$. The Q value and binding-energy are 31.53 ± 0.37 Mev and 5.61 ± 0.39 Mev respectively, if one assumes that the hyperfragment is a $_{\Lambda}Li^{7}$. On the other hand, if one assumes that it is a $_{\Lambda}Li^{8}$ hyperfragment, then the Q value and binding-energy are 31.48 ± 0.37 Mev and 5.66 ± 0.39 Mev respectively. Comparing these binding energies with the binding-energies determined by the Chicago group in their world survey, leads us to consider this hyperfragment as a $_{\Lambda}Li^{8}$.

2. Event 2B170-65. This hyperfragment has the same decay mode as the preceding lithium event. In this case the energy was apportioned among the three decay products in such a way that the recoil fragment had a range of 5.2 microns. We calculated the expected ranges for various light nuclei, assuming the recoil balances the pion and proton momenta. For Li^6 and Li^7 we calculated ranges of 6.3 and 5.6 microns respectively. Li^7 fits the measured range best, therefore we concluded that the hyperfragment is $_{\Lambda}Li^8$ and decays by the mode,

$$_{\Lambda}Li^8 \rightarrow \pi^- + H^1 + Li^7 + Q.$$

The Q value is 31.68 ± 0.37 Mev and the Λ^o-hyperon binding energy is 5.46 ± 0.40 Mev. The mean value of the binding energies of this event and the preceding event is 5.56 ± 0.28 Mev.

Event L95-19. This hyperfragment has a range of 5.6 microns and decays into three prongs: a singly charged prong of 283 microns range, a doubly charged prong of 230 microns, and a proton of range 29.34 mm. The event appears to be almost coplanar, therefore we tried all possible mass assignments for the prongs. We were unable to balance momentum for any of the assumptions. We next assumed that one neutron was emitted in the decay process. Under such an assumption, we obtained results that are fairly unambiguous. For the Q value of the reaction we get 148.9 ± 2.3 Mev, and for the binding energy of the Λ^o hyperon we obtain 8.9 ± 2.3 Mev. It should be pointed out that there is no guarantee that only one neutron was emitted in the decay, and if two were emitted, it is impossible to determine a unique binding energy. The hyperfragment identity and its decay mode are

$$_{\Lambda}Be^9 \rightarrow H^3 + He^4 + H^1 + n + Q.$$

The IBM 650 data-processing machine proved invaluable in making these calculations. We have attempted the analysis of selected non-mesonic hyperfragment decays using this IBM 650 machine, but in general the results of such an analysis are too ambiguous.

Binding Energies of Λ^0 Hyperons in Hyperfragments

In summary we list in Table V the binding energies that we have observed. These can be compared to the list of binding energies in the world survey--which includes our events--provided one adds 0.24 Mev to all their binding energies. For the Q of the free Λ^0-hyperon decay Levi Setti, Slater, and Telegdi use 36.9 Mev, whereas we use the value 37.14 Mev.

For these mesonic-hyperfragment decays, the errors in the binding energies are due almost entirely to the range straggling of the pions. More events are needed to reduce the errors. If there are excited states of hyperfragments, many more events will be needed to separate these excited states from their ground states. More information concerning the angular distribution of the pions from the mesonic-hyperfragment decays would be most helpful in understanding the Λ^0-nucleon interaction in these hyperfragments. The analysis of the nonmesonic hyperfragment decays would be desirable also, but in general, this would contribute little to the accuracy of the binding energies of the Λ^0 hyperons in the hyperfragments. A neutral particle is almost always associated with the nonmesonic decay modes, and the errors in direction measurements contribute strongly to the binding-energy errors (note our nonmesonic $_{\Lambda}Be^9$ event).

TABLE V

Binding energies observed for Λ^0 hyperons in hyperfragments.

Hyperfragment	Binding Energy (Mev)	No. of Events
$_{\Lambda}H^3$	-1.08 ± 0.72	1
$_{\Lambda}H^4$	1.56 ± 0.65	2
$_{\Lambda}He^4$	2.43 ± 0.56	1
$_{\Lambda}He^5$	2.66 ± 0.41	2
$_{\Lambda}Li^8$	5.56 ± 0.28	2
$_{\Lambda}Be^9$	8.9 ± 2.3	1

ACKNOWLEDGMENTS

I am especially grateful to Dr. Walter H. Barkas for having suggested this research and for his helpful guidance. I am deeply appreciative of the interest and encouragement of Dr. Robert Thornton.

I wish to thank Dr. Charles E. Violet for suggesting the use of the IBM 650 for hyperfragment analysis and for loaning us a copy of his program. I also wish to thank Mr. Victor O. Brady for writing a new IBM 650 program which proved to be very useful.

I am grateful to the scanners who found the hyperfragments and to Miss Hester Lowe who aided in the measurements on the hyperfragments.

Mr. Jim Hodges was most helpful in the construction of the nuclear-track photometer.

I should like to thank the members of the film group and the Bevatron crew, and all those who helped develop the K^--meson beam at the bevatron.

This work was done under the auspices of the U. S. Atomic Energy Commission.

APPENDICES

I. Angle Error Evaluation

The factor $\sqrt{\pi/4}$ which appeared in the section dealing with angle measurements is derived as follows. Consider a particle initially moving along the x axis. After traversing a distance x it is found at point A (see Fig. 9). In measuring its direction we place the line of a reticule along the track in such a way that it passes through O and A. Then $\sqrt{\langle \theta^2 \rangle}$ is the error in the measurement of the direction angle, where θ is the angle between the line OA and the x axis.

In Fig. 10 we show a track with tangents (dashed lines) at C and D and with equal chords BC and CD. The angle θ in this figure has the same significance as θ in Fig. 9. Here α is the absolute value of the angle between successive chords. From Fig. 10 we see that we have

$$\alpha = \theta + \phi,$$

therefore

$$\alpha^2 = \theta^2 + \phi^2 + 2\theta\phi.$$

There is a symmetry in Fig. 10 that allows the elimination of ϕ from the above expression. It makes no difference whether the track passes through C from the right or left, i.e., there is a right-left symmetry at point C with respect to the labeled quantities. If we form $\langle \alpha^2 \rangle$, then we have

$$\langle \alpha^2 \rangle = \langle \theta^2 \rangle + \langle \phi^2 \rangle ,$$

because $\langle \theta\phi \rangle = 0$ from the symmetry. In addition, the symmetry requires

$$\langle \theta^2 \rangle = \langle \phi^2 \rangle,$$

so that we have

$$\langle \alpha^2 \rangle = 2 \langle \theta^2 \rangle . \qquad (2)$$

Since α is distributed according to a gaussian, we also have

$$\langle \alpha^2 \rangle = \frac{\pi}{2} \langle \alpha \rangle^2 . \qquad (3)$$

Eliminating $\langle \alpha^2 \rangle$ between Eqs. (2) and (3) gives

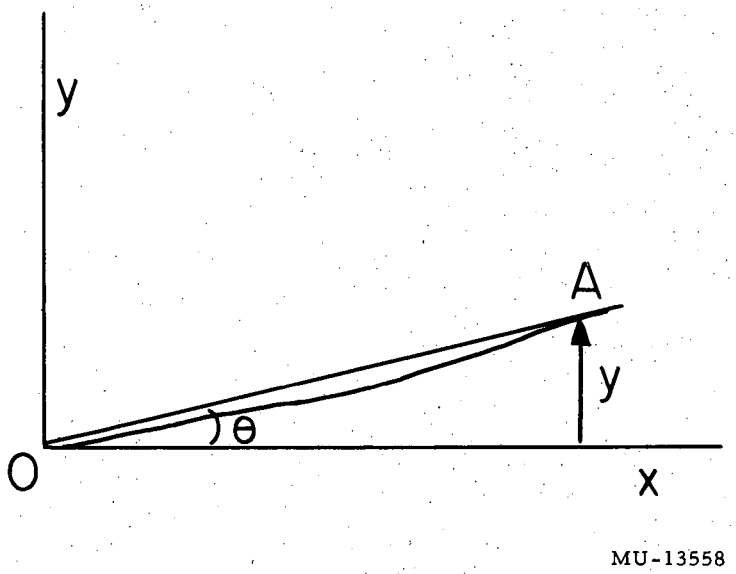

Fig. 9. Measurement of the direction of a track that multiply scatters in emulsion.

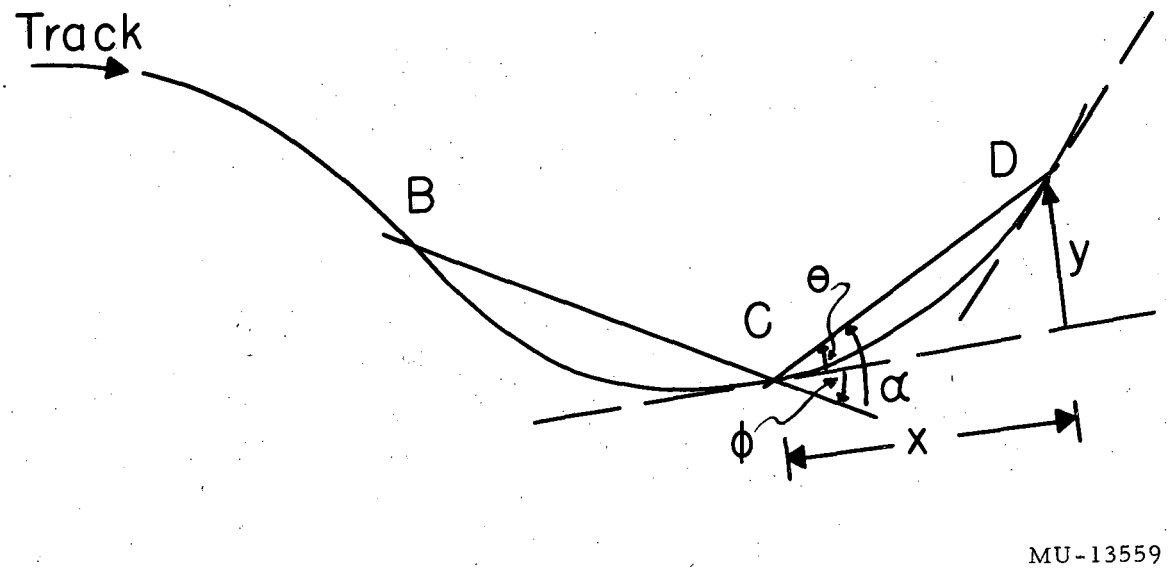

Fig. 10. Geometric relation between multiple scattering and the error in direction measurement of a track in emulsion.

$$\left\langle \theta^2 \right\rangle = \frac{\pi}{4} \left\langle a \right\rangle^2$$

or $$\sqrt{\left\langle \theta^2 \right\rangle} = \sqrt{\frac{\pi}{4}} \left\langle a \right\rangle ,$$

which is the desired expression.

The observer error, $\sigma_o = 17/t$, contains a factor 17, which we have estimated as follows: a reticule of length t is placed along a track of finite width. The accuracy with which the reticule can be aligned along the center of the track of finite width is limited by the angle whose tangent we estimate to be $0.3/t$, where t is in microns. The number 0.3 represents the half width of the track in microns. We make a small angle approximation and multiply 0.3 by $180/\pi$ to obtain the angle error in degrees, i.e.,

$$\sigma_o \cong \tan \sigma_o = 0.3/t,$$

or $\sigma_o = 17/t$, where σ_o is in degrees. The observer error σ_o and the multiple-scattering error σ_{ms} can be contained:

$$\sigma = \sqrt{\sigma_{ms}^2 + \sigma_o^2} ,$$

where $$\sigma_{ms}^2 = \frac{K^2}{(p\beta)^2} \frac{t}{100} ,$$

$$\sigma_o^2 = (17)^2/t^2 .$$

To find that length of reticule to be used in the angle measurement which gives the least error, we take

$$\frac{d\sigma}{dt} = \frac{1}{2} \frac{\frac{K^2}{100(p\beta)^2} - \frac{2(17)^2}{t^3}}{\sqrt{\sigma_{ms}^2 + \sigma_o^2}} = 0 ,$$

i.e., $t_m^3 = 2(17)^2(100)(p\beta)^2/K^2$.

For $K = 25$ we have

$$t_m^3 = 92.48\ (p\beta)^2 ,$$

$$t_m = 4.52\ (p\beta)^{2/3} .$$

Substituting this value of t in the expression for σ gives us the error corresponding to this minimal condition in terms of the $p\beta$ of the particle:

$$\sigma = \frac{6.51}{(p\beta)^{2/3}} .$$

II. Nuclear-Track Photometer

It is desirable to have some measure of ionization for slow particles in emulsion. Because of saturation effects in G.5 emulsion, it is impossible to make grain counts or gap counts that are very meaningful. Several workers in the field of nuclear track emulsion have shown that the width of the track is a measure of ionization.[16, 17] Some make these measurements with an eyepiece micrometer, while others make photomicrographs of the track and measure the width on the photomicrographs. Others project the image of the track and measure it with a scale. All these visual measurements involve a subjective factor, which is somewhat undesirable. The need for an objective measurement of track width led a number of workers to build photometers that measured the width of a track.[21-27]

We approached the problem in a way that was similar in principle to the approach by Professor Sten von Friesen and his co-workers.[22] Figure 11 shows the apparatus. A synchronous motor is geared to drive the x-screw of the miscroscope stage. A gear arrangement allows selection of three speeds: 5 microns sec^{-1}, 2.5 microns sec^{-1}, and 1 micron sec^{-1}. The optical system of a binocular microscope has been altered in the following ways: (a) one of the eyepiece tubes has the 1P28 photomultiplier mounted on it, and (b) in this same eyepiece tube is mounted a plane-parallel piece of glass which can be rocked back and forth about an axis perpendicular to the eyepiece tube. This is shown in greater detail in Fig. 12. As this plane-parallel glass rocks back and forth it causes the image to be displaced because of the refraction of the light passing through the glass. This glass piece is rocked through a cam arrangement by a synchronous motor at

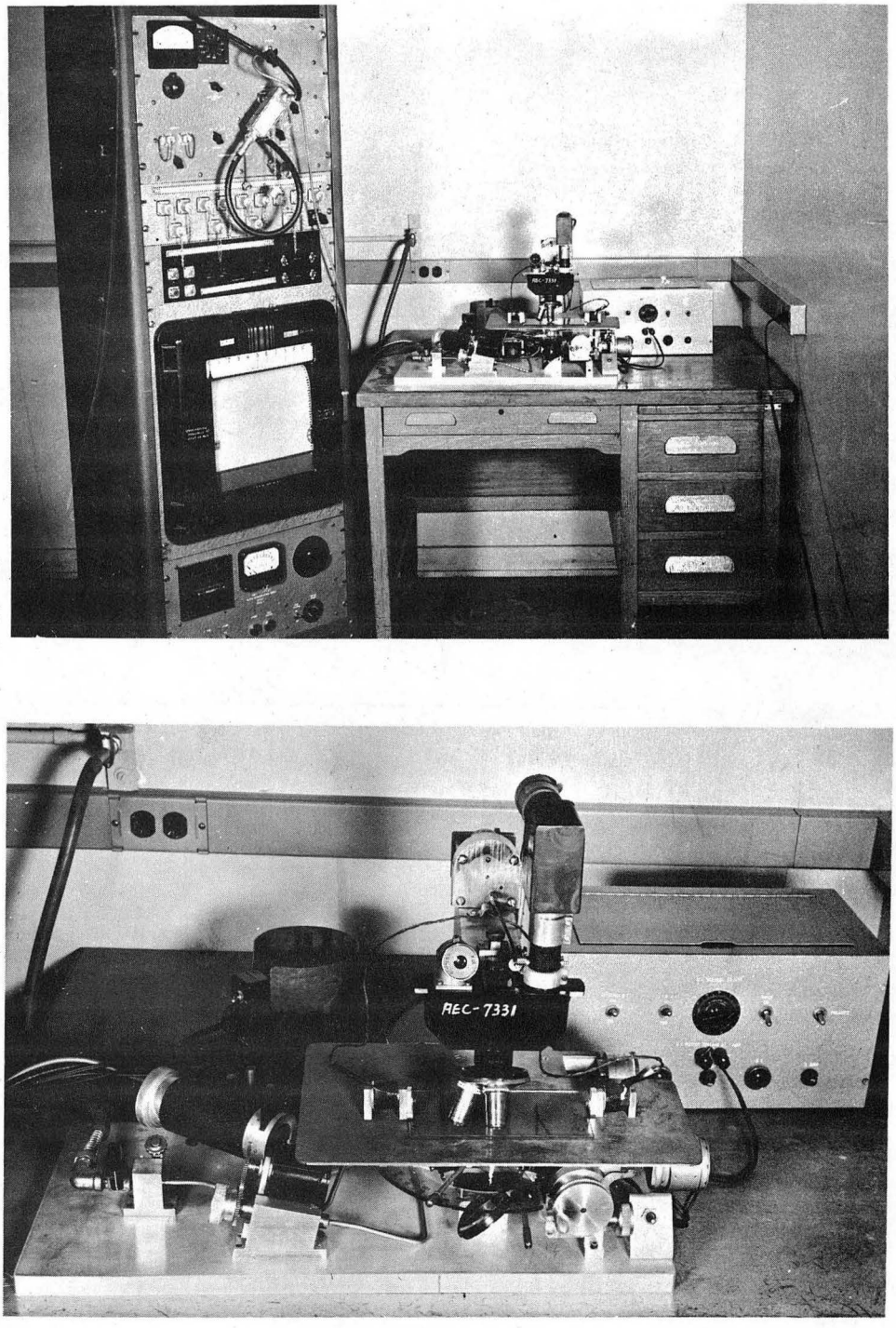

ZN-1734

Fig. 11. Nuclear-track photometer.

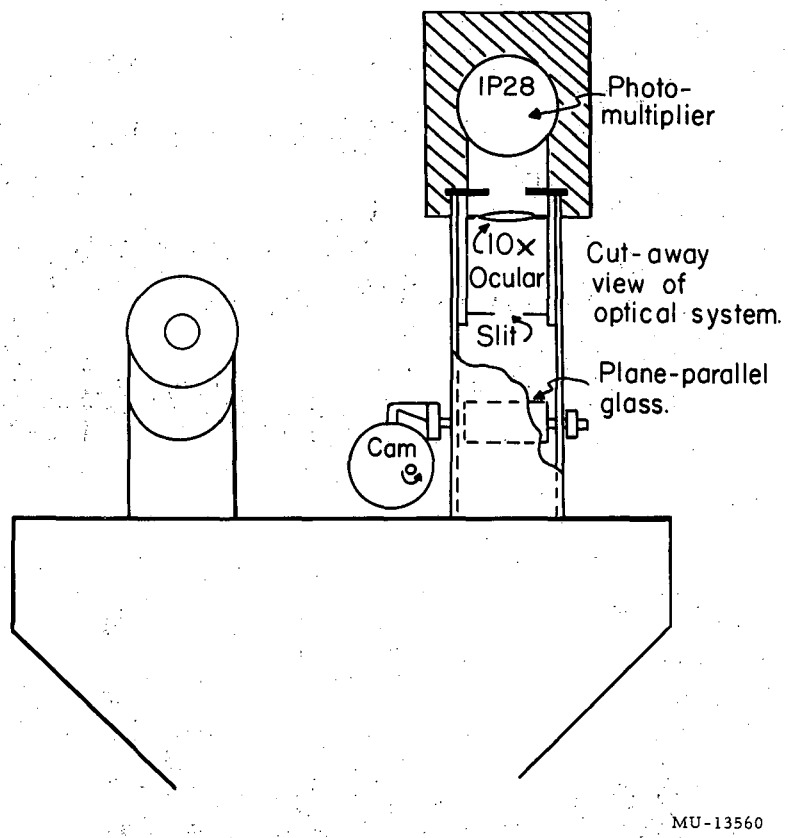

Fig. 12. Details of the optical system of the nuclear-track photometer.

a rate of 1 cycle per 8 seconds. The other eyepiece tube has a mirror arrangement in order that the eyepiece tube can be bent to a more comfortable scanning position. Referring again to Fig. 13, we see that the photomultiplier views the image of the microscope through a slit, which is placed in the reticule position of the ocular. The emulsion is placed on the stage in such a way that the track to be measured is parallel to the x axis. The motor on the x axis moves the track along its length and the rocking plane-parallel glass in the eyepiece tube causes the image of the track to be swept back and forth in the y direction across the slit through which the photomultiplier looks. This action is represented in Fig. 13. The signal from the photomultiplier passes to a dc amplifier and from there to a Leeds and Northrup Speedomax chart recorder. The chart is moved by a synchronous motor. Because of the use of synchronous motors throughout, the displacement of the chart paper bears a direct relation to the range of the track being scanned.

There are several features of the photometer that are worth mentioning. We have devised a hydraulic z-axis motion. The control under the left side of the stage is the Z screw, which moves a piston in a cylinder. The fluid pressure is transmitted through the copper tubing to a cylinder-and-piston arrangement on the head of the microscope. One of the reasons for using this type of z drive was the need for a vernier control of the z motion. One turn of the z control represents a z motion of about 30 microns. Mounted on top of the z control is a variable resistor which is geared to the z control. A battery supplies a voltage to the resistor and the position of the z-coordinate corresponds to a fraction of the battery voltage. This voltage is recorded periodically on the chart recorder and provides a record of the z-coordinate. Another feature incorporated on this microscope is a plate rotator. While following tracks, we find it necessary to reorient the emulsion in order that the track remain parallel to the x axis. A rotation about the optic axis is called for, and is done on this microscope in the same way as on the Koristka microscope. A sleeve, which is mounted on the condenser-lens support,

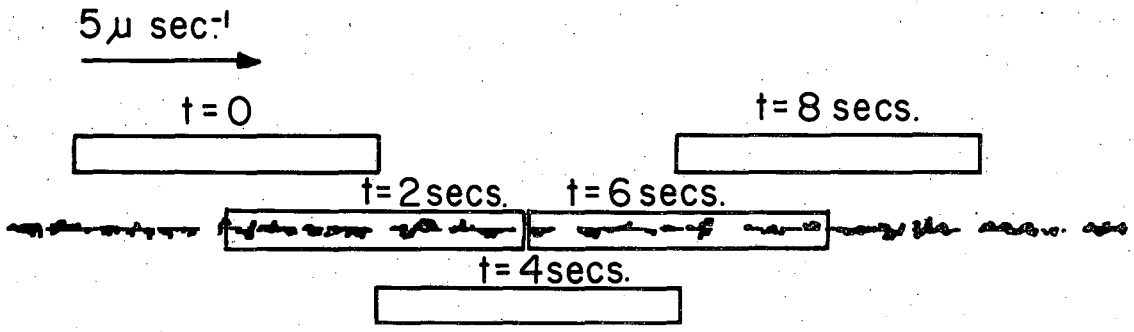

MU-13561

Fig. 13. Motion of the slit relative to the track in the nuclear-track photometer. The slit is 20 microns long and 2.5 microns wide.

can be raised until it touches the bottom side of the plate. A vacuum line to the sleeve provides a means for clamping the plate. The sleeve, with plate clamped on by vacuum, is raised further until the plate clears the stage, and then is rotated the necessary amount. We use electromagnets to hold the plate to the steel stage of the microscope, in order that the rotations may be made rapidly.

Measuring technique.

The operator aligns the plate in such a way that the track to be measured is parallel to the x axis. The motors are started and the operator controls two movements. The tracks must be kept in focus with the z control, and the track must be kept within certain limits in the y direction as the track is measured. Limits are scribed on the reticule of the observer's eyepiece, and with the y-screw he keeps the track within those limits.

Data reduction.

A typical chart record is shown in Fig. 14. The points C and D represent the light reaching the photomultiplier when the track is not in the image contained within the slit. Point B represents the light reaching the photomultiplier when the track is in the image contained by the slit. The quantity that is taken as significant is the ratio

$$S' = \frac{C + D - 2B}{C + D} .$$

This ratio must be corrected by a factor that depends upon the depth in the emulsion. The contrast of a microscope image depends upon depth in the emulsion and upon the general background in the emulsion. The periodic recording of the z coordinate allows such a correction to be made. Points Z in Fig. 14 are the z coordinates at those times. Figure 15 shows such a correction curve for a selected emulsion, in which protons and K mesons were studied. We have normalized the z correction to 1 at the surface of the emulsion. The ratio S' is to be divided by the correction factor. The correction curve is determined by measuring a number of proton endings at various depths in the

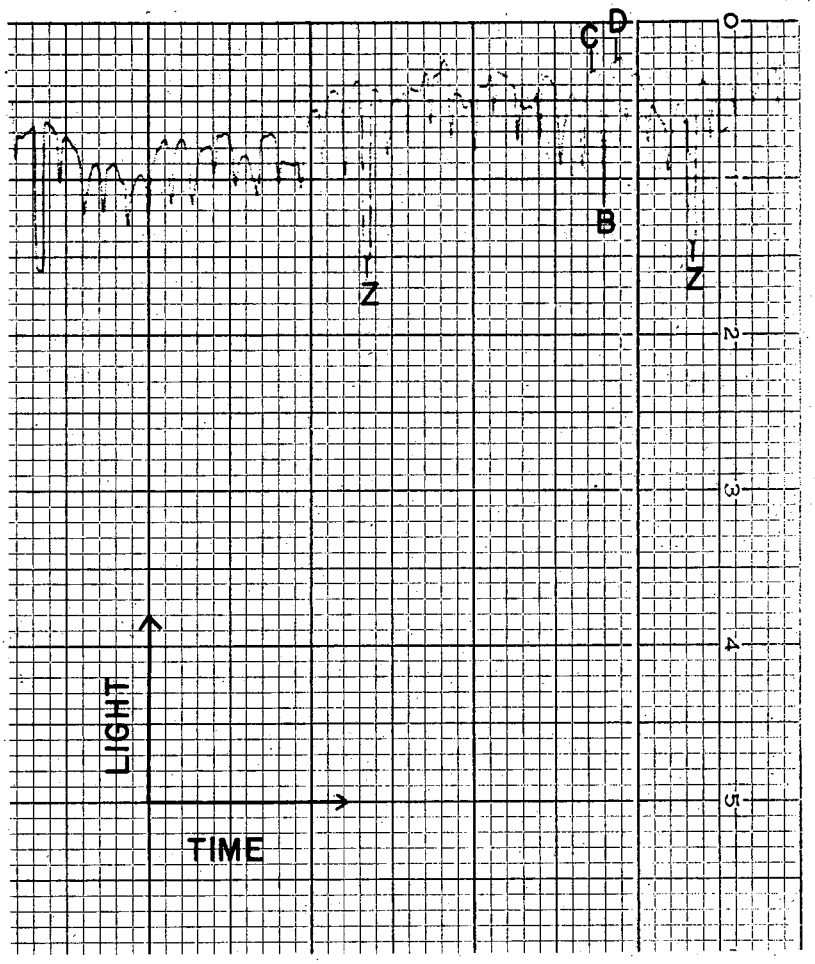

MU-13566

Fig. 14. Typical chart record of the nuclear-track photometer.

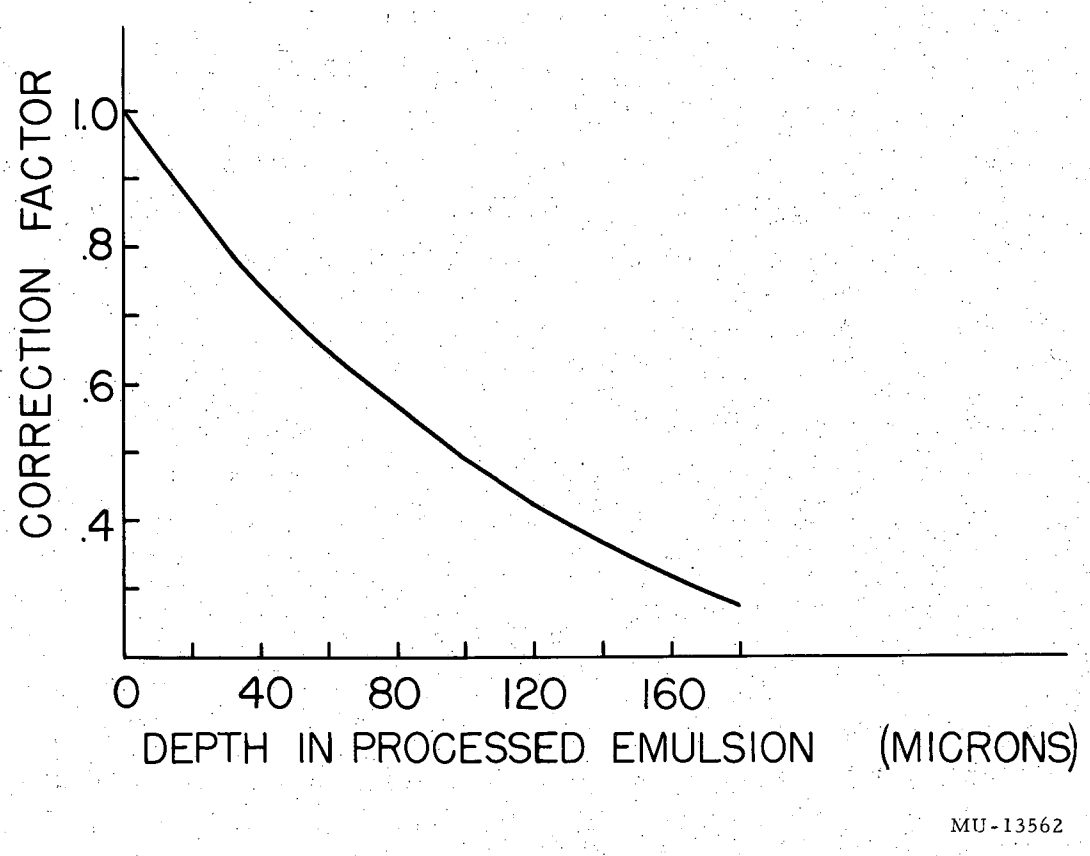

Fig. 15. Depth calibration curve for correcting photometric measurements according to depth in emulsion. This particular curve is for the emulsion used in the measurements indicated in Fig. 16.

emulsion. This z-correction curve must be established for each emulsion. As a means of evaluation of the method, we measured three proton tracks and four K-meson tracks. For this study we chose slit dimensions (in the image of the microscope) of 2.5 by 20 microns. We have integrated the track width graphically in Fig. 16. It is seen that the two groups begin to diverge at about 700 microns. A complete separation is obtained at about 900 microns.

Charge measurements.

We have changed the dimensions of the slit to 1.2 by 5 microns (in the image of the microscope), and used the photometer for comparative measurements on short multiply charged prongs from an interesting hyperfragment decay. The photometer was not used on any of the identified events.

Discussion of the photometer.

Certain features of the photometer make it a less precise instrument than one might first expect. The quantity S' is quite dependent upon the general background of the emulsion in the region where it is measured. We have grids printed on the underside of our emulsions in order that tracks can be followed from one pellicle to another. The values of S' are different when the image is above a grid number than when the image is not above a grid number. This suggests that it is impossible to make a reliable measurement of ionization for a long track, because of the crossing of grid numbers and lines. This limits our use of the instrument to short tracks. It seems that the instrument should be quite useful in determining the charge of short tracks. In addition, the determination of the z correction becomes troublesome because it must be done for each emulsion. Various methods of making ionization measurements, including the photometric method, have been studied by S. Nilsson.[28] The reader is referred to his paper for a quantitative comparison of these methods. From our studies, and from the paper by S. Nilsson, we believe the photometric method is most useful for saturated or nearly saturated tracks.

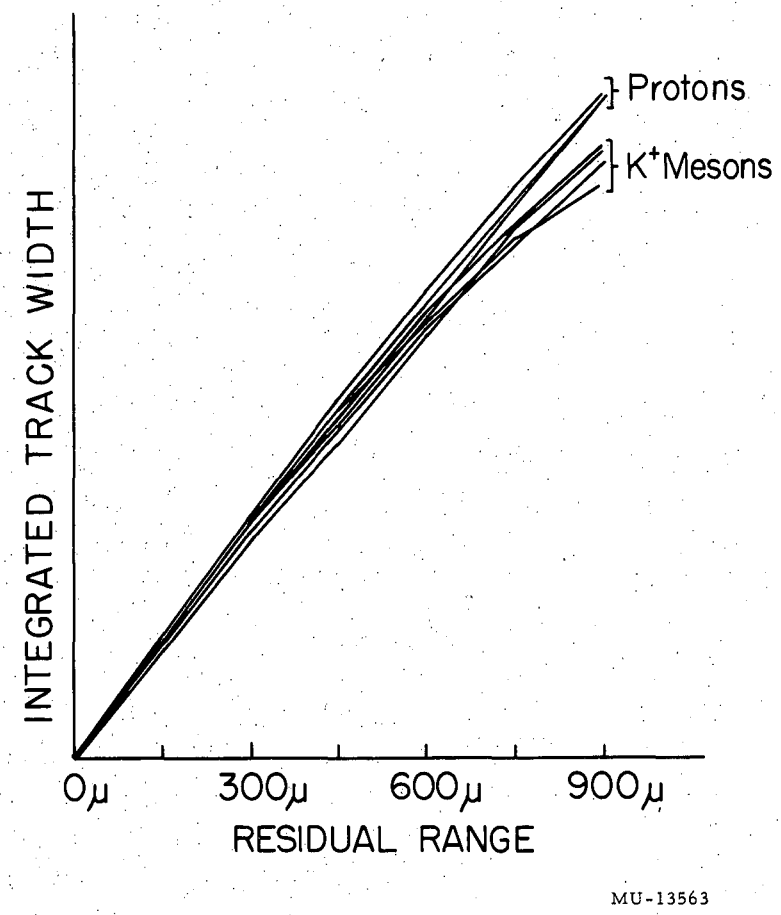

Fig. 16. Integrated track width vs residual range for three proton and four K-meson tracks in emulsion.

III. The IBM 650 Program for Hyperfragment Analysis

The program described in the following paragraphs has been used in the detailed analysis of selected hyperfragment decays. The idea of using the IBM 650 for hyperfragment analysis was first developed by Dr. Violet at Livermore. We have used a copy of his program, which he was kind enough to provide, and also written another program, which represents considerable improvement in machine time and ease of use. This second program is discussed in the following paragraphs.

In general, one cannot ascertain the identity of all the prongs from a hyperfragment decay without making a kinematic analysis of the decay. In practice, one assumes identities for each of the prongs and proceeds to calculate momentum balance, or unbalance, and visible energy release. Then one calculates from the energy release and the assumed identities a binding energy for the Λ^{o} hyperon. This binding energy must be positive. If in addition there is reason to believe that the decay does not involve a neutral particle (colinear or coplanar decays), momentum must balance. These two requirements are sufficient in many cases to allow identification of the hyperfragment.

The data for each hyperfragment decay are fed into the IBM 650 on punched cards. The first card contains two words of information. The first word tells the number of prongs from the decay. The second word contains information on whether or not a neutral particle is involved in the decay. If a neutral particle is involved, this word also tells what the particle is, e.g., one neutron, two neutrons, or a neutral pion. For example, suppose we have a hyperfragment that decays into two prongs which are obviously not colinear. Then we punch a number 2 in the first word of the prong-control card, and in the second word we punch a code number that might, for example, tell the machine to assume that the neutral particle was a pion.

A second card transfers control to the program. The reading of the first card is not a part of the program but just a memory-storage process.

Following these first two cards, the prong-control card and the transfer card, are the prong-data cards. Each prong of a hyperfragment decay has one card which contains the raw data applying to that prong. For a hyperfragment decaying into three prongs, there are three prong-data cards. Each of the prong-data cards contains the following information: R, ΔR, θ, $\Delta\theta$, δ, $\Delta\delta$, T, ΔT, and Z; where R is the range of the prong in millimeters, θ is the projected angle in degrees, δ is the dip angle in degrees, T is the energy in Mev, and Z is the charge. The Δ's refer to the errors associated with the various quantities. (We will refer later to the T and ΔT entries on the prong-data cards, since it appears redundant to list R and ΔR, as well as T and ΔT.) For each of the prongs we calculate the quantities

$$\lambda_\ell = \frac{R\ 938.232}{M_\ell (\text{Mev})} - Z^3\ (1.2 \times 10^{-4}),$$

where the subscript on the M permutes among the isotopes corresponding to the Z that was punched on the prong-data card for that prong. For example, if the machine finds a 1 punched for Z on the prong-data card, then the machine calculates 3 λ's, using the masses of the three hydrogen isotopes. After the machine obtains the λ's, it makes a linear interpolation between entries in a λ vs τ table--which is stored in the memory--and determines a τ for each of the λ's. These τ's are used to calculate T's corresponding to the τ's, as follows:

$$T_\ell = \frac{M_\ell\ \tau_\ell}{938.232} .$$

From the T's we obtain momenta corresponding to each of the energies, T:

$$P_\ell = \sqrt{T^2 + 2M_\ell T} .$$

The errors in the T's and p's are calculated by forming $R + \Delta R$ and redoing the calculation to this point to obtain a set of energies $T + \Delta T$, and the corresponding momenta, $p + \Delta p$. Subtraction of T from its corresponding $T + \Delta T$ and p from its corresponding $p + \Delta p$ gives the desired errors. Unfortunately this method of obtaining the energy of

a prong in terms of its range, by making use of the table of λ vs τ breaks down for slow, multiply charged particles. For this reason we reserved space on the prong-data cards for entering T and ΔT. For such cases, zeros are punched for R and ΔR. This instructs the machine to look at T and ΔT and bypass the calculations involved in using the λ-vs-τ table. When the range entry on the prong-data card is nonzero, then the T and ΔT spaces are ignored by the machine.

Now the machine has determined the energy and momentum of each prong for all its possible identities. The machine next begins to combine the above energies and momenta in all their possible permutations. For example, suppose we have a hyperfragment decay with a pion, a proton, and a He^4. On the pion prong-data card a -1 is punched, and there is only one mass value corresponding to this charge, namely, the pion mass. On the second prong-data card a 1 is punched for Z, and there will be three energies and momenta for this prong corresponding to the three isotopes of hydrogen. For the third prong-data card a 2 is punched for Z, and there are three energies and momenta corresponding to the three isotopes of helium. The machine then makes all possible permutations of three prongs. In this case there are nine permutations. A shorthand notation will be useful in describing the remainder of the program. The subscript i refers to the prong and the subscript j refers to the permutation. In the example above, i runs from one to three; there are three prongs involved in the decay. The subscript j runs from one to nine; there are nine possible permutations of the prong identities. With this notation, it is possible to express the resolution of the momentum of each of the prongs into three orthogonal components using the angle information supplied:

$$P_{ij_x} = P_{ij} \cos \delta_i \cos \theta_i ,$$

$$P_{ij_y} = P_{ij} \cos \delta_i \sin \theta_i ,$$

$$P_{ij_z} = P_{ij} \sin \delta_i \ .$$

The errors in the trigonometric functions are calculated as follows:

$$\Delta (\sin \alpha) = \sin (\alpha + \Delta\alpha) - \sin \alpha,$$

$$\Delta (\cos \alpha) = \cos (\alpha + \Delta\alpha) - \cos \alpha.$$

If we assume that for a given prong the errors in projected and dip angle are independent, then we have

$$\frac{\Delta P_{ij_x}}{P_{ij_x}} = \sqrt{\left\{\frac{\Delta P_{ij}}{P_{ij}}\right\}^2 + \left\{\frac{\Delta (\cos \delta_i)}{\cos \delta_i}\right\}^2 + \left\{\frac{\Delta (\cos \theta_i)}{\cos \theta_i}\right\}^2} \ ,$$

$$\frac{\Delta P_{ij_y}}{P_{ij_y}} = \sqrt{\left\{\frac{\Delta P_{ij}}{P_{ij}}\right\}^2 + \left\{\frac{\Delta (\cos \delta_i)}{\cos \delta_i}\right\}^2 + \left\{\frac{\Delta (\sin \theta_i)}{\sin \theta_i}\right\}^2} \ ,$$

$$\frac{\Delta P_{ij_z}}{P_{ij_z}} = \sqrt{\left\{\frac{\Delta P_{ij}}{P_{ij}}\right\}^2 + \left\{\frac{\Delta (\sin \delta_i)}{\sin \delta_i}\right\}^2} \ .$$

The momentum unbalance, or neutral-particle momentum, is obtained from the

$$P_{j_x} = \sum_i P_{ij_x} \ , \quad P_{j_y} = \sum_i P_{ij_y} \ , \quad P_{j_z} = \sum_i P_{ij_z} \ .$$

The errors are

$$\Delta P_{j_x} = \sqrt{\sum_i (\Delta P_{ij_x})^2} \ ,$$

$$\Delta P_{j_y} = \sqrt{\sum_i (\Delta P_{ij_y})^2} \ ,$$

$$\Delta P_{j_z} = \sqrt{\sum_i (\Delta P_{ij_z})^2} \ .$$

Therefore the momentum unbalance is

$$P_j = \sqrt{(P_{j_x})^2 + (P_{j_y})^2 + (P_{j_z})^2} \ ,$$

and

$$\Delta P_j = \sqrt{(\Delta P_{j_x})^2 + (\Delta P_{j_y})^2 + (\Delta P_{j_z})^2} \ .$$

The vector sum of the momenta of all the prongs is displayed as a momentum unbalance, if the machine has been instructed that there are no neutral particles participating in the decay. If the machine has been told that a neutral particle is to be involved, then it calculates a kinetic energy corresponding to this vector sum of the momenta,

$$T_j = \sqrt{P_j^2 + M^2} - M \ ,$$

where M is the neutral-particle mass in Mev. The machine has been instructed on the prong-control card as to which of the neutral particles is to be used in this energy calculation. For the two neutrons, this energy represents a lower limit to the kinetic energy carried away by the neutrons. The error in this kinetic energy of neutral particles is given by

$$\Delta T_j = \sqrt{(P_j + \Delta P_j)^2 + M^2} - \sqrt{P_j^2 + M^2} \ .$$

The total kinetic energy released in the decay is

$$Q_j = \sum_i T_{ij} + T_j \ ,$$

with

$$\Delta Q_j = \sqrt{\Sigma (\Delta T_{ij})^2 + (\Delta T_j)^2} \ ,$$

where we assume ΔT_j is independent of the energies of the prongs. This is valid in general because the error in T_j comes primarily from the errors in the angle measurements. The binding energy of the Λ^o hyperon in the hyperfragment is

$$B_{\Lambda^o_j} = M_j \left(\sum_i Z_i \ , \ \sum_i A_{ij} - 1\right) + 1115 - Q_j - \sum_i M_{ij} \ ,$$

with

$$\Delta B_{\Lambda^o_j} = \sqrt{(\Delta Q_j)^2 + (.0256)} \ ,$$

where M_j ($\sum_i Z_i$, $\sum_i A_{ij}$-1) is the mass of the nucleus with atomic number $\sum_i Z_i$ and mass number $\sum_i A_{ij}$-1. In order to obtain a complete picture of each analysis we have instructed the machine to punch out the following quantities on answer cards: Z_i, A_{ij}, T_{ij}, ΔT_{ij}, p_{ij}, Δp_{ij}, p_{j_x}, Δp_{j_x}, p_{j_y}, Δp_{j_y}, p_{j_z}, Δp_{j_z}, p_j, Δp_j, T_j, ΔT_j, Q_j, ΔQ_j, $B_{\Lambda^o_j}$, $\Delta B_{\Lambda^o_j}$. These quantities are compared for all the j permutations. The requirements for identification of an event have been outlined earlier in this appendix. The above quantities provide the necessary information to make such an identification.

One difficulty in the use of the program is associated with the range-straggling error. The range straggling depends upon the mass of the particle, and since the permutations of a given prong identity involve a number of masses, the straggling error is correct for only one of the masses. However, the proper straggling is taken into account when the correct decay reaction is found from the set of permutations.

IV. Transformation to the Λ^o-Hyperon Inertial Frame

We have used a geometrical method for performing the transformations to the Λ^o-hyperon inertial frame. The largest β for the examples we used was 0.169. This corresponds to a γ of 1.0146. We treated all these transformations nonrelativistically (the pion energy and momentum enter relativistically, however).

Consider the vector diagram of the pion, proton, and Λ^o-hyperon momenta (Fig. 17). In the inertial frame of the Λ^o hyperon, the pion has a momentum $\overrightarrow{OC}$, where the point O is as yet unspecified. The point O is determined by calculating how the energy is divided between the pion and proton in the inertial frame of the Λ^o hyperon. In the inertial frame of the Λ^o hyperon, the proton energy is 943.50 Mev and the pion energy is 171.50 Mev, where we take the Λ^o-hyperon rest mass to be 1115 Mev. The Λ^o-hyperon momentum is divided between the two particles in proportion to their energies, i. e., 943.50/171.50 = OB/AO. The angles are then read off with a protractor. We have plotted in Fig. 18 the point C with respect to O for the six

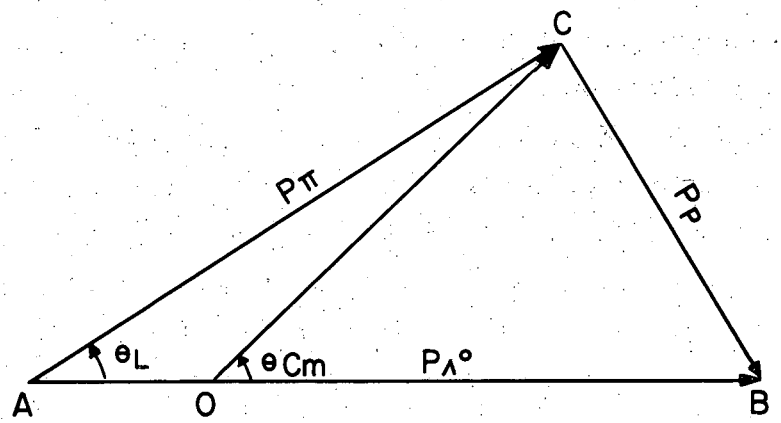

Fig. 17. Geometrical representation of the transformation to the inertial frame of the Λ^{o} hyperon in terms of the pion and proton momenta, p_{π} and p_{p}.

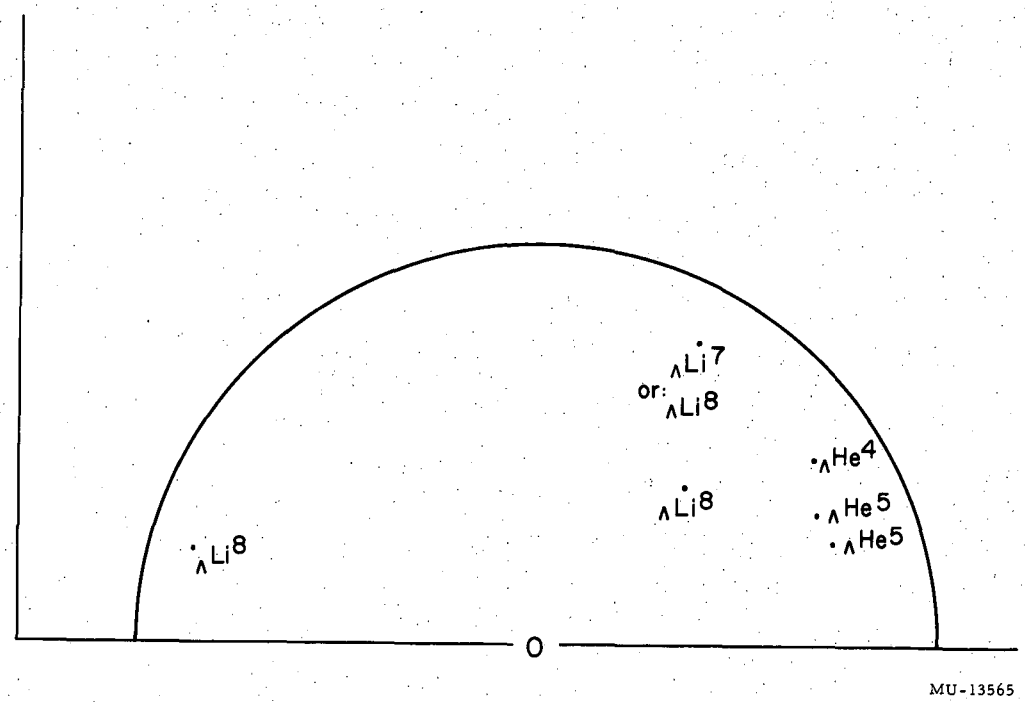

Fig. 18. Geometrical representation of the pion momenta for various hyperfragments. For a given hyperfragment, the pion vector momentum in the inertial frame of the Λ^0 hyperon is obtained by drawing a line from 0 to the point corresponding to the given hyperfragment.

cases we have analyzed. The semicircle represents the expected locus of points C for the decay of free Λ^o hyperons. The fact that our points all lie inside this semicircle is evidence for the binding of the Λ^o hyperons in the hyperfragments. An apparent Q value for the Λ^o-hyperon decay is calculated by attributing momentum OC to the pion and proton and calculating their energies. This was done, and the values are shown in Table IV.

BIBLIOGRAPHY

1. Danysz and Pniewski, Phil. Mag. 44, 348 (1953).
2. W. F. Fry, Proceedings of the Sixth Annual Rochester Conference on High-Energy Physics, 1956 (Interscience, New York, 1956).
3. Barkas, Dudziak, Giles, Heckman, Inman, Mason, Nickols, and Smith, Phys. Rev. 105, 1417 (1957).
4. W. F. Fry, J. Schneps, and M. S. Swami, Phys. Rev. 101, 1526 (1956).
5. H. Primakoff, Nuovo cimento 3, 1394 (1956).
6. T. K. Fowler, Phys. Rev. 102, 844 (1956).
7. G. Morpurgo, Nuovo cimento 3, 1069 (1956).
8. P. Zielinski, Nuovo cimento 3, 1479 (1956).
9. R. Levi Setti, W. E. Slater, and V. L. Telegdi, A World Survey of Experimental Data on Hypernuclei (1957) (hectographed preprint).
10. Malvin Ruderman and Robert Karplus, Phys. Rev. 102, 247 (1956).
11. J. Schneps, W. F. Fry, and M. S. Swami, Disintegration of Hyperfragments; III, to be published in Phys. Rev.
12. Filipkowski, Gierula, and Zielinski, Survey of the Hyperfragment Experimental Data, to be published in Acta Phys. Polon.
13. W. H. Barkas, The Range-Energy Relation in Emulsion, Part 2. The Theoretical Range, UCRL-3769, Apr. 1957.
14. Barkas, Smith, and Birnbaum, Range Straggling in Nuclear Track Emulsion, Phys. Rev. 98, 605 (1955).
15. W. H. Barkas and D. M. Young, Emulsion Tables I. Heavy-Particle Functions, UCRL-2579 (rev)., Sept. 1954.
16. Nakagawa, Tamai, Huzita, J. Phys. Soc. Japan 2, 191 (1956).
17. S. O. Sörensen, Univ. of Lund, private communication.
18. W. H. Barkas, and C. J. Mason, Bull. Am. Phys. Soc. 2, 235 (1957), and Seventh Annual Rochester Conference (1957).
19. Frank L. Adelman, Phys. Rev. 85, 249 (1952).
20. M. Gell-Mann and A. H. Rosenfeld, Annual Reviews of Nuclear Science (1957).

21. Blau, Rudin, and Lindenbaum, Rev. Sci. Instr. 21, 978 (1950).
22. S. von Friesen and K. Kristiansson, Ark. Fysik 4, 505 (1951).
23. M. Cecarelli and G. T. Zorn, Phil. Mag. 43, 356 (1952).
24. G. Kayas and D. Morellet, Compt. rend. 234, 1359 (1952).
25. M. Della Corte and M. Ramat, Nuovo cimento 9, 605 (1952).
26. P. Demers and R. Mathieu, Can. J. Phys. 31, 97 (1953).
27. L. van Rossum, Compt. rend. 236, 2234 (1953).
28. S. Nilsson, Arkiv Fysik 11, 201 (1957).